Journal of Energy Chemistry 24 (2015) 559–586

Contents lists available at ScienceDirect

Journal of Energy Chemistry

journal homepage: www.elsevier.com/locate/jechem

http://www.journals.elsevier.com/journal-of-energy-chemistry/

Review

Aligned carbon nanostructures based 3D electrodes for energy storage

Fengliu Lou, De Chen*

Department of Chemical Engineering, Norwegian University of Science and Technology, Sem Sælands vei 4, N-7491 Trondheim, Norway

ARTICLE INFO

Article history:
Received 15 July 2015
Revised 24 August 2015
Accepted 25 August 2015
Available online 3 September 2015

Keywords:
Aligned carbon nanostructure
Electrochemical energy storage
3D thin film nanoelectrode arrays
Metal foil
Electrochemical active material

ABSTRACT

Electrochemical energy storage systems with high specific energy and power as well as long cyclic stability attract increasing attention in new energy technologies. The principles for rational design of electrodes are discussed to reduce the activation, concentration, and resistance overpotentials and improve the active material efficiency in order to simultaneously achieve high specific energy and power. Three dimensional (3D) nanocomposites are currently considered as promising electrode materials due to their large surface area, reduced electronic and ionic diffusion distances, and synergistic effects. This paper reviews the most recent progress on the synthesis and application of 3D thin film nanoelectrode arrays based on aligned carbon nanotubes (ACNTs) directly grown on metal foils for energy storages and special attentions are paid on our own representative works. These novel 3D nanoelectrode arrays on metal foil exhibit improved electrochemical performances in terms of specific energy, specific power and cyclic stability due to their unique structures. In this active materials coated ACNTs over conductive substrate structures, each component is tailored to address a different demand. The electrochemical active material is used to store energy, while the ACNTs are employed to provide a large surface area to support the active material and nanocable arrays to facilitate the electron transport. The thin film of active materials can not only reduce ion transport resistance by shortening the diffusion length but also make the film elastic enough to tolerate significant volume changes during charge and discharge cycles. The conductive substrate is used as the current collector and the direct contact of the ACNT arrays with the substrate reduces significantly the contact resistance. The principles obtained from ACNT based electrodes are extended to aligned graphene based electrodes. Similar improvements have been achieved which confirms the reliability of the principles obtained. In addition, we also discuss and view the ongoing trends in development of aligned carbon nanostructures based electrodes for energy storage.

1. Introduction

The development of highly efficient, low cost, and environmentally benign electrochemical energy storage systems (ESS) is critical for addressing the urgent energy and environmental issues, and also plays a key role for the efficient utilization of renewable energy [1–7]. Supercapacitors (SCs) [8–11] and lithium ion batteries (LIBs) [12–17] have attracted considerable interest as ESS for applications in portable electronic devices and are being considered for electric vehicles and smart grid application. However, in order to meet the requirements of future applications, the next generations ESS are expected with higher specific energy and power, better cyclic stability, more safety, and lower cost [18]. Compared with LIBs, SCs can deliver a higher specific power, and offer a much better cyclic stability. However, LIBs exhibit much higher specific energy relative to SCs. Therefore, a major scientific challenge is to either significantly increase the specific energy of SCs or dramatically improve the specific power and cyclic stability of LIBs [19–21].

SCs are characterized by their specific power and cyclic stability resulted from the energy storage mechanism [19]. They can be categorized as electric double-layer capacitors and redox pseudocapacitors according to the energy storage mechanism [8]. The former as shown in Fig. 1 is based on physical charge separation at the electrode/electrolyte interface, while the latter utilizes fast and reversible redox reactions occurring at the electrode surface or subsurface. SCs show a higher specific power and better cyclic stability owing to the fast and reversible charge separation and surface redox reaction. However, they exhibit relatively lower specific energy compared with LIBs due to the surface energy storage mechanism. Previous attempts to increase the specific energy of SCs include the utilization of electrode materials with enhanced specific capacitances [23,24] and electrolyte with wider operation voltage window [25–27]. Therefore, carbon nanomaterials with large specific surface area [23], nanostructured transition metal oxides [28–31] and conducting polymers [32,33] with enhanced pseudocapacitance have attracted widespread interest for high specific energy SCs. The utilization of electrolyte with wide operation voltage window, such as

* Corresponding author.
E-mail address: chen@nt.ntnu.no (D. Chen).

http://dx.doi.org/10.1016/j.jechem.2015.08.013
2095-4956/

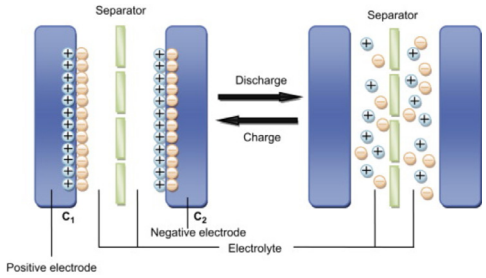

Fig. 1. Charged and discharged states of an electric double-layer capacitor [22].

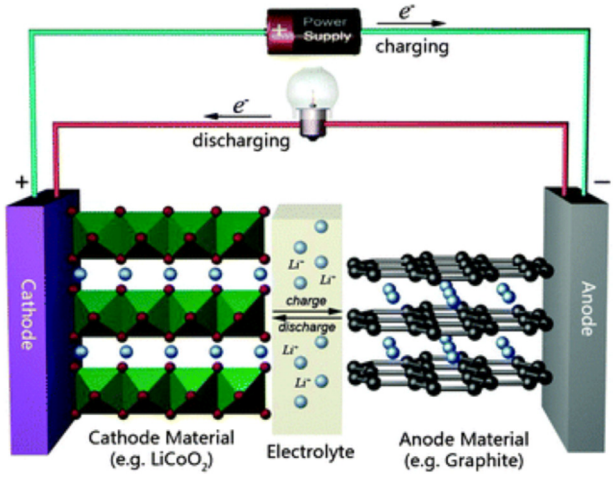

Fig. 2. Typical commercial LIBs showing the charge/discharge intercalation mechanism [6].

organic electrolyte and ionic liquid, is another route to increase the specific energy of SCs [25,26,34].

Typical LIBs comprise a negative electrode, a polymer separator permeated with non-aqueous liquid electrolyte, and a positive electrode (Fig. 2). Lithium ions are extracted from anode, transferred across the non-aqueous lithium ion containing organic electrolyte and intercalated into the cathode which is accompanying by the electrons transport from anode to cathode through the external circuit during discharge, and vice versa during charge. LIBs store electrochemical energy through Faradaic reactions in the bulk of the active material. This bulk energy storage mechanism provides a much higher specific energy as compared with SCs. However, storing lithium ions in the bulk of a material implies that lithium ions must transfer in the bulk electrode materials during charge and discharge. Because of the low solid state diffusion rates, this process is generally a rate limited step. As a result, LIBs deliver a very low specific power, requiring typically hours for charge and discharge. Additionally, due to a vast amount of side reactions occurring during overcharge or overdischarge which cause electrolyte decomposition, passive film formation, active material dissolution, and also other phenomena, LIBs suffer from capacity fading with cycling which results in poor cyclic stability [35].

The demand of safe ESS with large specific energy and high specific power is continuously increasing. Exploring full potential of present materials and searching for new electrode materials and electrolytes have been carried out around the world to improve the performance of present ESS [15]. One strategy to explore the full potential of present electrode materials is the fabrication of active materials into 3D nanostructures. This route can enlarge the specific energy of SCs by increasing specific surface area and improve the specific power of LIBs by reducing the lithium ion and electron diffusion distances. This review focuses on the applications of aligned carbon nanotubes (ACNTs) and aligned graphene based 3D electrodes for SCs and LIBs. We start with a discussion of the rational design of ESS, in terms of higher specific energy and specific power, and better cyclic stability, based on thermodynamic and kinetic analysis of elementary steps involved in the energy storage process (Section 2). The synthesis methods of ACNTs on metal foils and coating of thin layer of active materials such as conducting polymers and metal oxides, and their applications in energy storage are reviewed in Sections 3 and 4, respectively. Additionally, the latest progresses on aligned graphene for ESS have been summarized in Section 5. Finally, the ongoing trends of aligned carbon nanostructures based 3D electrodes for energy storages are discussed (Section 6).

2. Rational design

ESS involves a series of complex physical and chemical processes such as mass, ionic and electron transport, heat transfer as well as reactions in a multiphase system. Existing electrodes needs to be significantly improved in terms of such processes in order to meet future requirement. In this section, we will provide fundamental principles to achieve high specific energy and power from a chemical reaction engineering point view, by means of thermodynamic and kinetic analyses of the physical and chemical processes involved. We start to summarize fundaments of electrochemical processes in energy storage, although they can be found in many textbooks, to provide fundamental principles of rational design of electrodes.

2.1. Specific energy

2.1.1. Theoretical specific energy

The theoretical specific energy (E_{tse}) of SCs can be calculated according to the following equation:

$$E_{tse} = \frac{1}{2} C \Delta U^2 \quad (1)$$

where, C and ΔU are specific capacitance and maximum cell voltage, respectively [52]. Accordingly, the specific energy of SCs depends on the specific capacitance and the maximum operation voltage. The maximum operation voltage is limited by the stability of the electrolyte, which is beneath 1.23 V for aqueous electrolyte due to the hydrogen or oxygen evolution. The operation voltage window can be widened by employing organic electrolyte and ionic liquid up to around 3 and 4 V, respectively [26,34].

For SCs storing energy based on charge separation, the specific capacitance is measured as [43,53]

$$C = \frac{\varepsilon_r \varepsilon_0 A}{d} \quad (2)$$

where, ε_r, ε_0, A, and d are electrolyte dielectric constant, vacuum dielectric constant, specific surface area of the electrode materials, and the effective thickness of the electric double-layer, respectively. Therefore, a general strategy to increase the specific capacitance of an electrode material is to increase its effective specific surface area. Hence, many researches have been focused on the investigation of different high surface area carbon based materials for SCs, such as carbon nanotubes, graphene, active carbon and their composites [26,34,54].

Electric double-layer capacitance is present in any electrochemical cell. In the case of an electrode material also exhibiting a pseudocapacitance, the pseudocapacitance is coupled in a parallel way with electric double-layer capacitance [8]. Therefore, the theoretical specific capacitance of electrode material participating redox reaction can be estimated by the contributions from both the electric double-layer and the faradic redox reaction according to Equation (3) [33],

$$C = \frac{\varepsilon_r \varepsilon_0 A}{d} + \frac{nF}{M \Delta U} \quad (3)$$

Table 1. Properties of typical electrode materials used for SCs.

Material	Electronic conductivity (S/cm)	n[a]	Operation voltage (V)	Theoretical capacitance[b] (F/g)	Refs.
Carbon	10^0 to 10^1	–	–	15–30 μF/cm^2	[36, 37]
SnO_2	10^2	1	1	640	[38, 39]
Fe_2O_3	10^{-5}	1	0.7	863	[40, 41]
MnO_2	10^{-6} to 10^{-5}	1	0.9	1233	[42]
NiO	0.01 to 0.32	1	0.5	2584	[43]
CoO	10^{-9}	2	0.6	4292	[44, 45]
Co_3O_4	10^{-4} to 10^{-2}	4	0.45	3562	[43]
V_2O_5	10^{-4} to 10^{-2}	4	1	2122	[43]
RuO_2, H_2O	10^0 to 10^3	18/7 to 30/7	1.229	1336–2227	[43, 46]
$Co(OH)_2$	-	2	0.6	3460	[47]
$Ni(OH)_2$	-	1	0.5	2081	[48]
Polyaniline	4.4	1	0.9	1178	[33, 49]
Polypyrrole	0.07 to 90.49	0.33	0.8	594	[49, 50]
Poly(3,4-ethylenedioxythiophene)	10^0 to 10^2	0.33	1.2	187	[51]

[a] n refers to the number of moles of electron transferred per mole of reactants.
[b] The theoretical specific capacitance is calculated according to $C = nF/(M\Delta U)$, without considering double-layer contribution. 96485 C/mol was selected for Faraday constant.

Table 2. Properties of typical electrode materials used for LIBs.

Application	Material	Electronic conductivity (S/cm)	Li^+ diffusion coefficient (cm^2/s)	Average voltage (V vs Li^+/Li)	Theoretical capacity (mAh/g)	Refs.
Cathode	$LiCoO_2$	10^{-4}	10^{-10} to 10^{-8}	3.9	274	[59,60]
	$LiMn_2O_4$	10^{-6}	10^{-11} to 10^{-9}	4.1	148	[60]
	$LiFePO_4$	10^{-9}	10^{-15} to 10^{-14}	3.45	170	[60,61]
	$LiCo_{1/3}Mn_{1/3}Ni_{1/3}O_2$	10^{-6}	10^{-11} to 10^{-10}	3.8	278	[62,63]
	$LiNiO_2$	10^{-4} to 10^{-3}	10^{-9} to 10^{-8}	3.7	275	[64]
	LiV_3O_8	10^{-4}	10^{-10} to 10^{-8}	2.8	280	[65,66]
	Li_2FeSiO_4	10^{-14}	10^{-12} to 10^{-10}	2.5	332	[67]
	MnO_2	10^{-6} to 10^{-5}	10^{-11} to 10^{-9}	3.0	308	[68]
	S	10^{-30}	10^{-16} to 10^{-15}	2.2	1675	[69–71]
Anode	graphite	10^3	10^{-10} to 10^{-8}	0.1	372	[59,60]
	$Li_4Ti_5O_{12}$	10^{-10}	10^{-17} to 10^{-14}	1.7	175	[72,73]
	MnO_2	10^{-6} to 10^{-5}	10^{-11}	1.1	1233	[74]
	Fe_2O_3	10^{-6} to 10^{-5}	10^{-12}	1.7	1005	[75,76]
	Si	10^{-5}	10^{-11}	0.4	4200	[77]

transition metal oxides, such as Co_3O_4, NiO, V_2O_5, RuO_2, MnO_2, and conducting polymers, such as polyaniline and polypyrrole would be good candidate materials as electrodes for SCs based on their high specific capacitances as shown in Table 1 [33,43].

The maximum electrical work available from a LIBs cell is determined by thermodynamics, which equals to the Gibbs free energy of the discharge reaction under standard condition ΔG, as shown in the Nernst equation [55]:

$$\Delta G = -nFE^0 \tag{4}$$

where, n refers to the number of moles of electron transferred per mole of reactants, F is the Faraday constant, and E^0 is electromotive force. Therefore, the theoretical specific energy, the theoretical energy that can be derived per unit mass of the active electrode materials [56], can be calculated according to Equation (5) [16]:

$$E_{tse} = \frac{-nFE^0}{\sum M_i} \tag{5}$$

where, ΣM_i is the sum of the formula mole weights of active materials being transformed in the discharge reaction. Therefore, in order to achieve high specific energy, the cell should assembled based on the cathode and anode with more electrons transferred per molecule of active materials, large potential difference to generate a high voltage, and lighter molecular weights [16]. The amount of charge produced, nF, can be considered to be a capacity factor, while the electromotive force, E^0, can be thought of as an intensity factor [57]. For a given electrode material, the theoretical specific capacity can be calculated from the following equation [58]:

$$Q = \frac{nF}{3.6M} \tag{6}$$

oxides with high number of electron transferred per mole of reactants (n) could yield a high theoretical specific capacity. Conducting polymer has been proved to provide high specific capacity due to its low molecular weight (M). The theoretic specific capacities of some typical electrode materials used for LIBs are summarized in Table 2.

2.1.2. Practical specific energy

The practical specific energy (E_{pse}) can be calculated by integrating the discharge current and the corresponding voltage over a whole discharge cycle,

$$E_{pse} = \frac{\int_0^{\Delta t} IU_{dis}dt}{m} \tag{7}$$

where, I, U_{dis}, t, and m are discharge current, discharge voltage, discharge time and mass of electrode materials, respectively. The practical specific energy is always lower than the theoretic value, which is limited by the accessibility of active sites resulted from inefficient electron and/or ionic transport and the lower operating voltage due to overpotentials, as illustrated in Fig. 3.

For carbon based electric double-layer capacitor, the high specific surface area electrode materials should be accessible for the ions from the electrolyte to achieve high specific capacitance [78]. Both the surface properties and pore size of the materials required to be optimized to maximize specific capacitance. For pseudocapacitors and LIBs, the effective specific capacitance or capacity depends on the volume ratio η [79,80],

$$\eta = 1 - \left(1 - \frac{L}{r}\right)^d \tag{8}$$

where, L is the ionic diffusion distance, r is the radius of the particle and d is determined from the dimension of the ionic mobility into the framework. In order to use the entire active materials to approach the

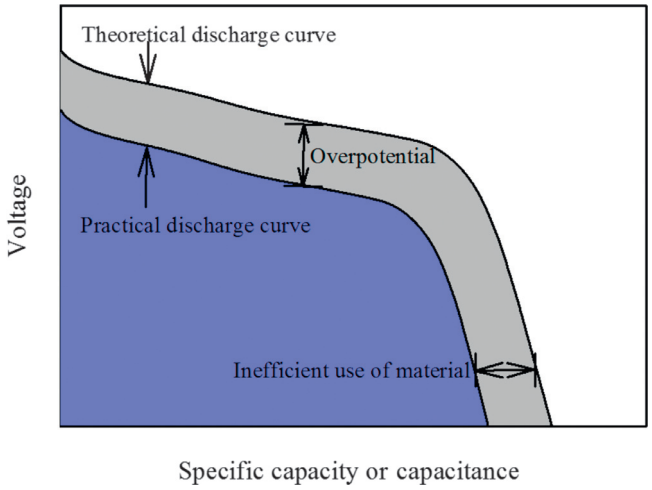

Fig. 3. Schematic illustration of the difference between practical specific energy and theoretical specific energy due to overpotential and inefficient use of electrode materials.

theoretical specific capacitance or capacity, the ionic diffusion distance L should be longer than particle radius r.

The discharge voltage U_{dis} is always lower than the electromotive force E^0 due to polarization [60],

$$U_{dis} = E^0 - \eta_a - \eta_c - \eta_r \quad (9)$$

where, η_a, η_c, and η_r are overpotential caused by activation, concentration, and resistance polarization, respectively. Activation polarization arises from kinetics barriers of the charge transfer reaction taking place at the electrode/electrolyte interface. It can be described by the Tafel equation [56,81],

$$\eta_a = (RT/\alpha nF) \ln (i/i_0) \quad (10)$$

where, α is transfer coefficient, i is current density, and i_0 is exchange current density. Concentration polarization results from limited mass transport capabilities which can be expressed as [57]

$$\eta_c = (RT/nF) \ln (C/C_0) \quad (11)$$

where, C and C_0 are the concentration at the electrode surface and in the bulk of solution, respectively. Resistance polarization originates from the resistance of the electrolyte, electrode materials, current collectors, and contact between them. Resistance polarization follows Ohms's Law [57],

$$\eta_r = IR_\Omega \quad (12)$$

where, R_Ω is internal resistance which is affected by the conductivity of the electrode materials and electrolyte and their interfaces [60]. These overpotentials should be minimized to heighten the discharge voltage, thus achieving high specific energy.

2.2. Specific power

The specific power, P, is the speed of energy that can be derived per unit mass of active materials which can be calculated according to Equation (13),

$$P = U_{dis} I/m \quad (13)$$

Therefore, it depends on the discharge voltage and discharge current for a given cell. Accordingly, the improvement in specific power requires the development of ESS with low internal resistance, fast redox reaction, and rapid mass transfer to maximize the discharge current while limit the overpotentials within an acceptable level. The internal resistance arises from the Ohmic resistance of different steps in the discharge process. The activation process and mass transfer cause charge transfer resistance and mass transfer resistance, respectively. Additionally, one more process needs to be considered for LIBs, namely, the immigration of lithium ion through the solid electrolyte interface (SEI) which causes SEI resistance. The information about different resistances can be extracted from electrochemical impedance spectra based on their different time constants.

Nyquist plots of different ESS and corresponding typical equivalent circuits are given in Fig. 4, where the characteristic behaviors are depicted. The first figure (Fig. 4a) represents the behavior of an ideal electric double-layer capacitor, which can be described by an internal resistance (R_Ω) in series with an electric double-layer capacitance (C_{dl}) [8,37]. However, a real electric double-layer capacitor cannot be described by one *RC* circuit but a succession of *RC* components in series or in parallel (transmission line model [82]) (Fig. 4b). The presence of Warburg region (45° region) at high frequencies is a result of the distribution of resistance/capacitance in a porous electrode [83]. The transportation of ions from electrolyte to the external surface induces a resistance (R_1) and charges the corresponding surface which produces a capacitance (C_1). The transportation of ions into the internal surface leads to another resistance (R_2) and capacitance (C_2). This can be repeated again and again along the electrode pore until the bottom of the electrode is reached [84]. The deviate from vertical line at the low frequency region is due to a distribution in macroscopic path lengths, or a distribution in microscopic adsorption process, or electrode roughness [37,83]. The behavior of pseudocapacitors with mass transfer limitation is shown in Fig. 4(c), which can be described by a modified Randles' equivalent circuit [37,85]. It consists of an internal resistance (R_Ω), a double-layer capacitance (C_{dl}) in parallel with a pseudocapacitive branch. The pseudocapacitive branch consists of a charge transfer resistance (R_{ct}) which is related to the redox reaction, a pseudocapacitance (C_{ps}), and a Warburg element (Z_w) which accounts for the charge diffusion in the active materials [37]. In addition to the internal resistance (R_Ω), double layer capacitance (C_{dl}) and charge transfer resistance (R_{ct}) caused semicircle at medium frequencies, Warburg impedance (Z_w) caused sloping line at low frequencies, and intercalation capacitance (C_{int}) caused steeper sloping line at lowest frequencies, one more loop presents in the Nyquist plot at high frequencies for lithium ion half-cell as a result of lithium ion migration through the SEI film caused corresponding capacitance (C_{SEI}) and resistance (R_{SEI}) (Fig. 4d) [59,86,87].

2.2.1. Internal resistance

The internal resistance is the sum of various Ohmic contributions in the system, such as electronic resistance (active materials, conductive additives, percolation network of additives in electrode, current collector, and electrical taps), ionic resistance (electrode and electrolyte), and the interfacial resistance (between the different components in the cells) [60,84,88]. It can be obtained from the real-axis intercept of the Nyquist plot at high frequency. The internal resistance can be reduced by improving the electronic conductivity of the electrode and the ionic conductivity of the electrode and electrolyte, and enhancing the interfaces between electrode, electrolyte, and current collectors.

2.2.1.1. Electronic resistance. Electrons transport from the active sites through the electrode, current collector, external circuit, and another electrode to the active sites of another electrode during operation, therefore the electronic resistance is of critical importance for high power ESS. However, most electrode active materials are semiconductors or insulators (Tables 1 and 2). Hence, the improvement of electronic conductivity is necessary to enhance the cell performance. As a result, many researchers have focused on improving electronic conductivity of electrode by surface coating or introducing conductive additives into the electrode materials [88,89] and improving the intrinsic electronic conductivity of active material by doping [90,91]. Carbon [88,92–94], conducting polymer [95–98], and silver

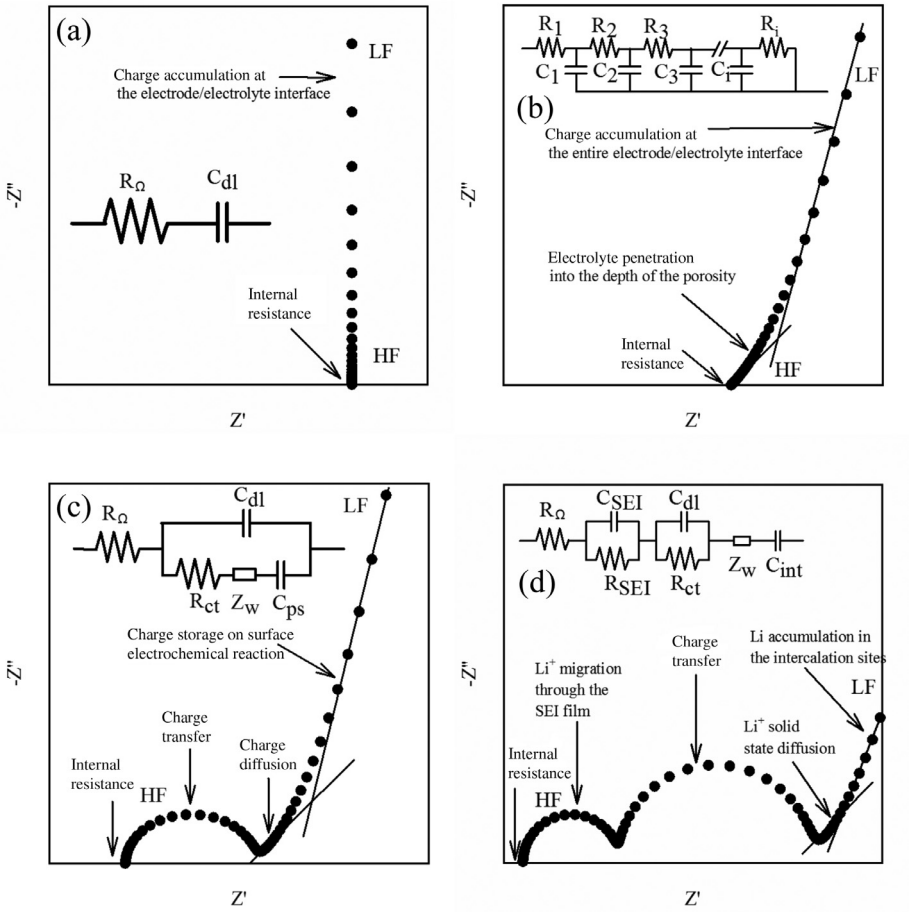

Fig. 4. Nyquist plot and corresponding equivalent circuits of (a) an ideal electric double-layer capacitor, (b) a real electric double-layer capacitor, (c) a pseudocapacitor, and (d) a lithium ion half-cell. HF: high frequencies; LF: low frequencies.

[99] etc. have been investigated as conductive coating layer to increase the electronic conductivity of active materials. The electronic conductivity of active materials improves significantly after conductive film coating and shows improved specific capacity and markedly enhanced rate capability as electrodes for LIBs. Highly conductive carbon, such as acetylene black [100], carbon nanotubes [101], and graphene [102–104], etc. are often incorporated into active materials as conductive additives to facilitate the electron transport. Additionally, the electronic conductivity of $LiCoO_2$ has been increased by over two orders of magnitude up to about 0.5 S/cm by partial substitution of Co^{3+} by Mg^{2+} and compensating hole creation by West et al. [91]. Besides, Hüseyin Göktepe reported the improvement of electronic conductivity of $LiFePO_4$ by Yb^{3+}-doping up to 1.9×10^{-3} S/cm [90].

2.2.1.2. Ionic resistance. The function of the electrolyte is to provide an ionic conduction path between electrodes. Therefore, the ionic conductivity is a critical property for electrolyte. The most widely used electrolytes are liquid solution containing ionic species in either aqueous or organic solvent (Table 3). Less conventional electrolytes consist of room temperature ionic liquids and solid state electrolytes. However, solid state electrolytes and aqueous electrolytes suffer from low ionic conductivity and limited voltage window, respectively [105]. Hence, organic solvent based electrolytes are widely used for practical ESS.

The electrolyte ionic conductivity can be calculated according to Equation (14). Accordingly, it is associated with the concentration and mobility of the dissolved ionic species. Dissociation of the salt is determined by the dielectric constant of the solvent, and a high value indicates strong solvating power. The motion of ions is influenced by the viscosity, and low viscosity facilitates ionic movement [60]. It is difficult for a single solvent to have both a high dielectric constant and a low viscosity and this is the reason why the electrolyte used in LIBs contains more than one type solvents.

$$\kappa = \sum_i \frac{Z_i^2 F C_i}{6\pi \eta r_i} \tag{14}$$

where, κ, Z, C, η, and r are electrolyte ionic conductivity, charge number, molar concentration, viscosity, and ion radius, respectively.

The ionic diffusion in electrode materials is associated with the ionic diffusion coefficient and the diffusion distance. The characteristic time for diffusion can be expressed as follows [80]:

$$\tau = \frac{L^2}{D_i} \tag{15}$$

where, L is ionic diffusion distance, which is relevant to the particle size of electrochemically active material, and D_i is the ionic diffusion coefficient. As a result, diffusion limitation of lithium ions may exist due to the intrinsic slow diffusivity of lithium ions in the solid state materials which are generally the rate determining step [88]. Therefore, nanostructures have a genuine potential to make a significant improvement on the rate capability of LIBs by reducing the lithium ion diffusion distance.

Table 3. Comparison of typical electrolyte properties.

Electrolyte	Operation window (V)	Viscosity (cP)	Ionic conductivity (mS/cm)	Dielectric constant	Safety	Refs.
Aqueous	1.23	0.88–10.91	up to 1000	about 80	high	[37,106,107]
Organic	2.5–3.7	0.45–3.2	0.24–19.40	2–90	low	[37,108–111]
Ionic liquid	up to 4–6	21–574	0.1–18	5–20	medium	[105,112,113]

All the data are reported at the room temperature.

2.2.1.3. Interfacial resistance. The interfacial resistance includes the resistances between electrodes and electrolyte, between active material particles and conductive additives, between electrode and current collector, and between conductive additives and current collectors [60]. Carbon black has been widely used as conductive additive to enhance the electrode conductivity which provides a point to point contact mode with active materials [114]. Recently, Li et al. reported two dimension carbon additive, namely graphene, shows lower contact resistance with $LiFePO_4$ than carbon nanotubes and carbon black due to the plane to point electrical contact mode [115]. Therefore, the contact resistance between conductive additives and active materials can be reduced with proper contact mode. The conventional electrodes are prepared by tape casting or roll to roll method to coat the active materials onto current collector which results in a large contact resistance between them [116,117]. This contact resistance can be significantly reduced by preparing active materials directly on current collector. Bordjiba el al. demonstrated that the contact resistance between the active material and the current collector was reduced due to the presence of carbon nanotubes [118].

2.2.2. Charge transfer resistance

Charge transfer resistance (R_{ct}) is the resistance of ion transferring from a solvated ionic state in the electrolyte crossing the electrode/electrolyte interface and inserting into the electrodes, which causes the activation polarization [119]. The charge transfer resistance can be studied using electrochemical impedance spectroscopy (EIS). The value can be extracted from the diameter of a semicircle in Nyquist plot at the medium frequencies. R_{ct} is dependent on the electrode properties according to the following relationships [81],

$$R_{ct} = \frac{RT}{nFAj_0} \tag{16}$$

$$j_0 = nFkC^m \tag{17}$$

where, A, j_0, k, c and m are electrode surface area, exchange current density, rate constant, concentration, and reaction order, respectively. The rate constant depends on the temperature, potential, and activation energy. The activation energy of charge transfer process represents the barrier that the ion needs to overcome to cross the electrode/electrolyte interface.

The charge transfer process consists of several elementary steps, but the solvation and desolvation process has been recognized as the rate determining step [120]. Therefore, it is necessary to reduce the activation energy of solvation and desolvation in order to improve the reaction kinetics at the interface. Nakayama et al. assumed that the charge transfer activation energy originates from the large energy mismatch between the chemical potentials at the bulk of the electrolyte and at the electrode and the chemical potential of lithium ion is mainly affected by the solvation of lithium ion in the electrolyte [120]. Accordingly, they coated a layer of polymer on the surface of electrode to reduce the activation energy. The results shown the activation energy was successfully reduced with the presence of a polymer layer via solvation and desolvation at two interfaces [120].

2.2.3. Mass transfer resistance

Electrolytes with low ionic transport numbers and salt diffusion coefficients may generate large concentration polarization during operation. This results in low specific power, unwanted side reactions and poor cyclic stability. It is therefore important to improve the mass transfer in electrolytes [121,122]. Mass transfer in solution occurs by diffusion, migration and convection, which can be described by Nernst–Planck equation [55,123],

$$J = -D\nabla C - \frac{zF}{RT}DC\nabla\phi + Cv \tag{18}$$

$$D = \frac{D'\varepsilon}{\tau} \tag{19}$$

where, J is the flux, C is concentration, z is the charge of species, ϕ is electric potential, v is the velocity which is zero for SCs and LIBs, ε is the porosity, and τ is tortuosity. D' and D are intrinsic and effective diffusion coefficient, respectively. Accordingly, the tortuosity of pores can be manipulated to increase the effective diffusion coefficient and thus specific power.

2.2.4. Solid electrolyte interface resistance

SEI film is normally formed between an electrode and the electrolyte arises from the decomposition of electrolyte mostly during the firstly several cycles [124]. It is a determinant factor on the performance of LIBs since it affects the rate capability, cyclic stability, and even safety [124]. This film should be not only ionic conductive, which allows lithium ions to be transported through it during the following charge and discharge process, but also electronic insulative, which prevents the further consumption of electrolyte [125]. It consists of a variety of solvent and salt decomposition products, such as lithium alkyl carbonate, lithium carbonate, depending on the composition of the electrolyte. The SEI film can be formed both on anode and on cathode in LIBs.

The lithium ion transfer through the SEI film could be rate determining step if it is poor ionic conductor and the lithium ion diffusion through the electrolyte and the bulk electrode materials are fast [126]. EIS has been identified as a powerful method to investigate the SEI film formation and evolution with cycling. The SEI resistance can be extracted from the diameter of a semicircle in Nyquist plot in the high frequencies (Fig. 4) [127].

2.3. Cyclic stability

The cyclic stability of ESS is closely related to physicochemical feature evolution of both electrode and electrolyte during cycling. Electric double-layer capacitor has extremely good cyclic stability when operated properly because the energy storage mechanism is only based on physical charge separation. However, pseudocapacitors which are based on the surface redox reaction of conducting polymers or metal oxides surfer from capacitance fading due to conducting polymers degradation caused by the break of polymer molecular backbones [128] or the irreversible reduction and morphology reconstruction of metal oxides [129]. LIBs surfer from capacity fading as well during cycling, which might be attributed to electrolyte decomposition, SEI film formation, active material dissolution and phase transformation, and mechanical stress caused segregation, as shown in Fig. 5 [35]. Therefore, both electrode and electrolyte need to be rationally designed to achieve high cyclic stability.

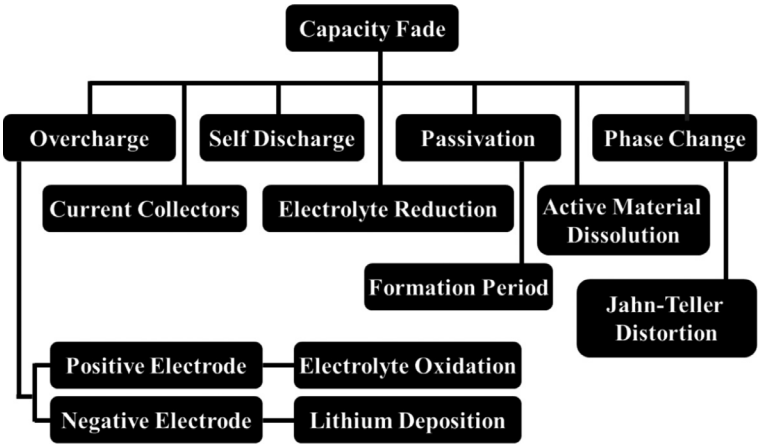

Fig. 5. Flow chart describing various capacity fade phenomena in LIBs [35].

The heat generated during charge and discharge process, which results in the temperature increases within the cell, would grow with the square of internal resistance according to the Ohm's law ($Q = IR_\Omega{}^2$). Higher operating temperature would accelerate the degradation of the cell life due to the decomposition of electrolyte, growth of SEI, dissolution of electrode materials, or phase transformation of electrode etc. [88,130–132]. In addition, the electrodes experience volume change during charge and discharge which would cause the segregation of the active materials. Therefore, the electrode resistance should be minimized to reduce the heat generated while the electrode void space requires to be optimized to release the mechanical stress generated due charge and discharge to improve the cyclic stability of the cells.

2.4. Design of high performance electrochemical energy storage systems

Based on above analysis, different resistances in the cell became critical to improve the specific energy, specific power, and cyclic stability of ESS. Therefore, the electrodes require to be rationally designed to reduce the resistances of mass and charge transfer as well as the internal resistance at different scales to optimize the performance.

For a given electrolyte system, one strategy to improve the mass transfer is to decrease the pore tortuosity. Tortuosity (pore path length per unit scaffold thickness) quantitatively describes the degree of pore straightness, which is equal to 1 for a straight pore. The value of tortuosity for ACNTs was found to be 1.3 when ions were transferred through the pore created between closely packed nanotubes [133]. This value is approaching the theoretical limit of 1 due to the perfectly straight pores [133]. However, the tortuosity for active carbon was found to be in the range of 7.9–15.6 in the same system [134]. Additionally, Hata et al. demonstrated the improvement of diffusion coefficient up to 20 times by utilizing ACNTs instead of activated carbon as electrode materials [133]. This indicates the fast mass transfer characteristic in the pores formed among ACNTs. The charge transfer resistance on the interface between the active materials and electrolytes could be reduced by means of coating of conducting polymer or carbon [120]. The improvement in specific power requires the development of cells with low internal resistances in addition to fast charge and mass transfer. The internal resistance with the sum of resistance of different steps in the discharge process should be minimized, which includes (i) the electronic resistance of the electrodes, (ii) the ionic diffusion resistance in the electrodes, (iii) ionic diffusion resistance in electrolyte, and (iv) the interfacial resistance between the electrodes and the current collectors and between the electrodes and the electrolytes [22,59,60,135].

The strategy of nanostructured hybrid electrodes satisfies well the requirement of improved kinetics owing to short charge diffusion distance, void space for enhancing mass transfer, synergistic effects, as well as high specific surface area. Therefore, as presented in Fig. 6, various types of 3D nanostructured electrodes have been investigated for high performance ESS, including nanotube arrays [136–138], nanotube film [139,140], nanosheet arrays [141,142], nanosheet film [143,144], mesoporous materials [70,145], etc.

Among them, the 3D coaxial core/shell nanoarrays grown directly over conductive substrates have been investigated intensively due to their unique structures resulted high performance [32,33,146,147]. The nanoarrays were grown directly over conductive substrate which reduces the interfacial resistance between current collector and active materials because the arrays adhere robustly to the substrate. The core in the core/shell arrays generally has high electrical conductivity which results in the low electrode resistance. The regular mesopores among the nanotubes reduce the tortuosity and thus improving the mass transfer in the electrolyte. The high specific surface area of core could server as support for the deposition of shell materials which are generally electrochemically active materials. It allows to keep the thin film, but with a high loading of active materials. The thin film of active materials shortens the ionic diffusion distance which enhances the utilization efficiency of the active materials as well as reduces the ionic diffusion resistance in the electrodes. These rationally designed electrodes could heighten the specific energy and enhance the specific power. Moreover, this is a kind of polymer binder and organic solvent free electrode preparation methods which simplifies the electrode preparation and reduces the environmental impact.

Tarascon et al. firstly reported the deposition of Fe_3O_4 over copper nanoarrays as anode for LIBs and 80% of the total capacity can be achieved at 8 C, indicating excellent rate capability [138]. Recently, MnO_2/Mn/MnO_2 sandwich-like nanotube arrays have been prepared for SCs [148]. The crystalline metal Mn layers serve as highly conductive cores to support the redox active two-double MnO_2 shells with a highly electrolytic accessible surface area and provide reliable electrical connections to MnO_2 shells. Additionally, Fan et al. reported the preparation of ZnO/MnO_2 and Co_3O_4/MnO_2 core-shell arrays on stainless steel substrate to functionalize as pseudocapacitor electrodes [31,149]. Besides, Cui et al. designed one dimensional MnO_2/titanium nitride nanotube coaxial arrays for a high performance electrochemical capacitive energy storage system [150]. However, both the complicated preparation processes and the high material cost limit the widespread application of these core-shell arrays, although excellent electrochemical performances have been achieved.

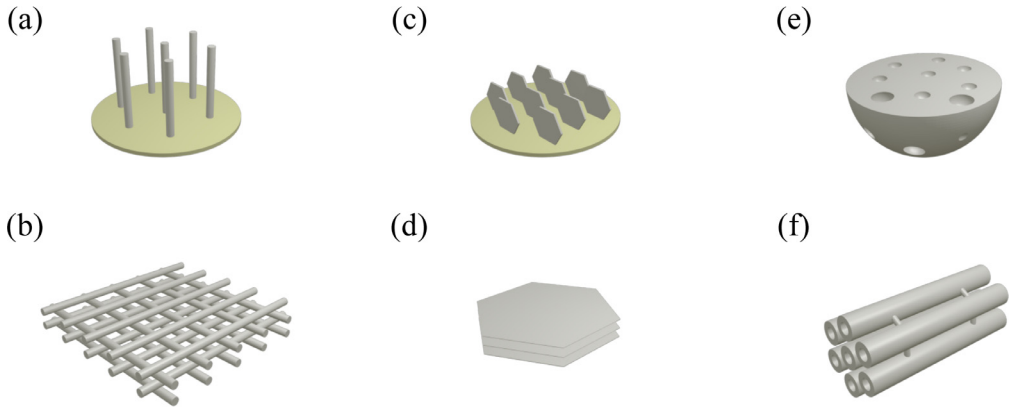

Fig. 6. Three dimensional nanostructures investigated as electrodes for energy storages. (a) Nanowire/nanotube array, (b) nanowire/nanotube paper, (c) nanosheet/nanowall array, (d) nanosheet/nanowall paper, (e) hierarchical porous materials, (f) ordered mesoporous materials.

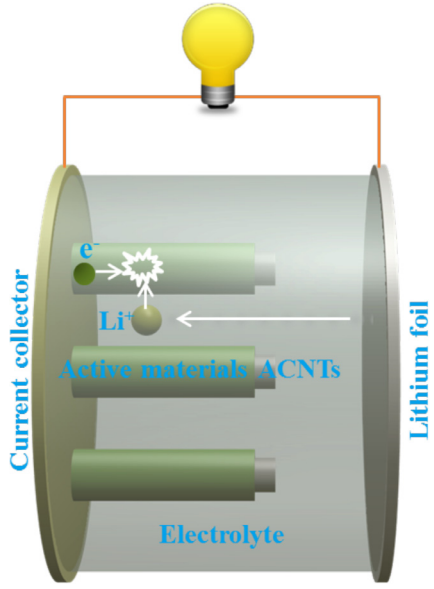

Fig. 7. Schematic illustration of the discharge process of ACNTs/metal foil based electrodes for a lithium ion half-cell.

On the contrary, 3D electrodes based on ACNTs on metal foils attract increasing interest due to their high electrical conductivity, corrosion resistance, high specific surface area, and facile fabrication. Various active materials have been deposited over ACNTs for energy storage, such as MnO_2 [146,147], polyaniline [32,33], Si [151,152], sulfur [69] etc. Fig. 7 demonstrates the discharge process of an ACNTs/metal foil based electrodes for lithium ion half-cell. The lithium ion diffuses fast among the strait channels formed between nanotubes to the active materials and inserts into the active materials which is accompanied by the transport of electron from the external circuit to the current collector and through the highly conductive ACNTs to the conduction band of active materials. Then the electron and lithium ion diffuse within a short distance to the active sites. The low resistances of different steps involved in the discharge process guarantee the high performance of the obtained cells.

3. Synthesis of aligned carbon nanotubes and their composites

3.1. Synthesis of aligned carbon nanotubes over conductive substrates

ACNTs can be synthesized by a variety of methods, such as cutting carbon nanotubes/polymer composite [153], growth confinement [154,155], template assisted method [156], chemical vapor deposition [157], floating catalyst method [158] etc. However, the application of ACNTs as electrodes for energy storage requires ACNTs contact directly with conductive substrates [158]. Therefore, the synthesis of ACNTs directly over conductive substrates attracted intensive interest recently [147,158].

3.1.1. Template assisted method

ACNTs can be synthesized by utilizing anodized aluminium oxide (AAO) as template through chemical vapor deposition for carbon coating within the pores [159]. AAO is selected due to its facile synthesis, controllable pore size, well ordered pores, and the highly dense pores along with its amenable ability to be dissolved in either acidic or basic solutions [160]. In brief, one side of the alumina template is coated with a layer of conductive material firstly (Fig. 8b), which will serve as the conductive current collector. Then carbon is subsequently coated on the interior of the perfect aligned channels through chemical vapor deposition to form well-ordered ACNTs (Fig. 8c). Finally, alumina template is removed with either acidic or basic solutions (Fig. 8d). ACNTs synthesized by this method are characterized by their open end and perfect hollow cylinder structure, which are challenges for other methods [161]. The ACNTs can be employed to encapsulate active materials for energy storage which can improve the electronic conductivity due to the presence of highly conductive carbon nanotubes and cyclic stability by restricting the dissolution of active materials [161–163]. Ajayan's group has done a lot of pioneering works on the synthesis of ACNTs by using AAO template assisted method for energy storage [164–167]. However, there are many limitations for this method, including high cost, low productivity, complex process, and discharge of waste water.

3.1.2. Multi-step chemical vapor deposition

ACNTs/conductive substrate can also be synthesized *via* multi-step chemical vapor deposition methods, including transfer of the as-prepared ACNTs from non-conductive substrates to conductive ones and the growth of ACNTs on conductive substrates with pre-deposited catalyst film (Fig. 9a).

With the development of chemical vapor deposition techniques, ACNTs can be facilely synthesized over non-conductive substrate with high quality at very fast growth rates [168]. Hence, one possible approach for the preparation of ACNTs/conductive substrates is the transfer of the as-synthesized ACNTs from non-conductive substrates to conductive ones. Zhang et al. demonstrated the transfer of ACNTs from silica substrate to nickel foam by utilizing a cut-paste method as electrodes for SCs [169]. The obtained electrodes show a low specific capacitance of 14.1 F/g but excellent rate capability. Honda et al. also reported the preparation of ACNTs/conductive substrates by

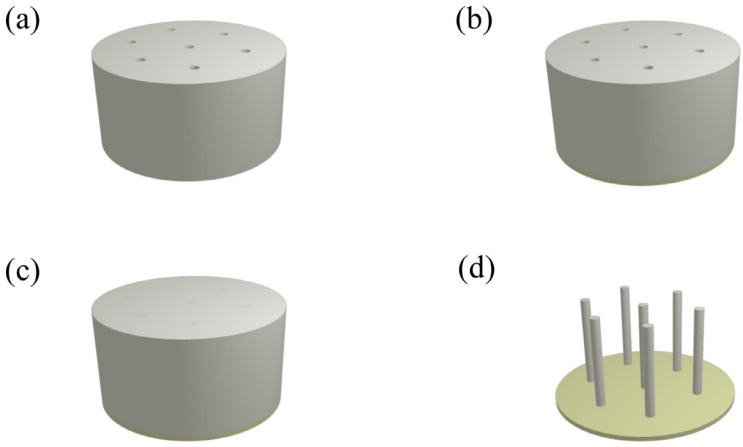

Fig. 8. Schematic illustration of the synthesis of ACNTs/conductive substrate utilizing template assisted method. (a) Anodized aluminium oxide, (b) anodized aluminium oxide/conductive substrate, (c) carbon coated anodized aluminium oxide/conductive substrate, (d) ACNTs/conductive substrate.

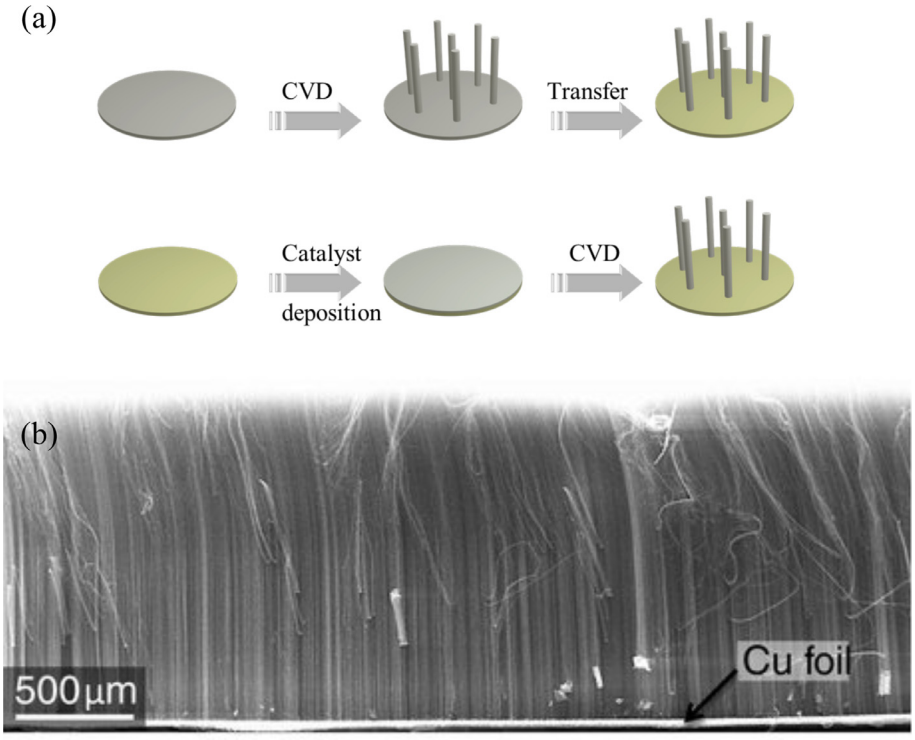

Fig. 9. (a) Schematic illustration for the growth of ACNTs over conductive substrate using multistep method. (b) SEM image of a ACNTs based thick electrode adhered onto a thin copper foil [151].

transferring ACNTs from silicon substrate to an aluminum foil for an electric double-layer capacitor [170]. ACNTs up to 1 mm in length were synthesized via low pressure chemical vapor deposition process by Gleb Yushin et al. (Fig. 9b) [151]. Then ACNTs were adhered to a thin copper foil through thermal process after Si coating. The obtained active materials demonstrate very good stability for over 250 cycles and high specific capacity approaching theoretical limits of Si as anode for LIBs. Besides, ACNTs with length up to 0.9 mm have been synthesized through chemical vapor deposition over alumina coated Si wafers by Chen et al [171]. Mn_3O_4 nanoparticles were then homogenously deposited within the highly dense, millimeter long ACNTs by dip-casting method from non-aqueous solutions after ACNTs were removed from the substrate. Finally, a thin Au layer was sputtered on the back of the ACNTs which served as current collector. The specific capacitance of ACNTs@Mn_3O_4/Au film composites is found to be 143 F/g in an aqueous electrolyte of 0.5 M Na_2SO_4.

A thin layer of transition metal film can be deposited over conductive substrate, such as metal and graphene film, as catalyst for the growth of carbon nanotubes before chemical vapor deposition process. Many techniques have been employed for the fabrication of this catalyst film, such as electron beam evaporation [172,173], sputtering coating [174], dip-coating [172], spin coating, spray coating [175] etc. An alumina buffer layer is usually required to prevent the dissolution of metal catalyst into substrate [176] and alloy formation with the substrate or tune the interaction between catalyst and substrate [158]. Zhang et al. reported the growth of ACNTs over Ta foil with an alumina buffer layer [147,177]. However, the alumina buffer layer deposited between the conductive substrate and catalyst film weakens the electrical contact and mechanical adhesion between ACNTs and the conductive substrates. Additionally, the incompatible thermal expansion coefficients of alumina and metal may also lead to detaching of the ACNTs and the alumina buffer layer from the conductive

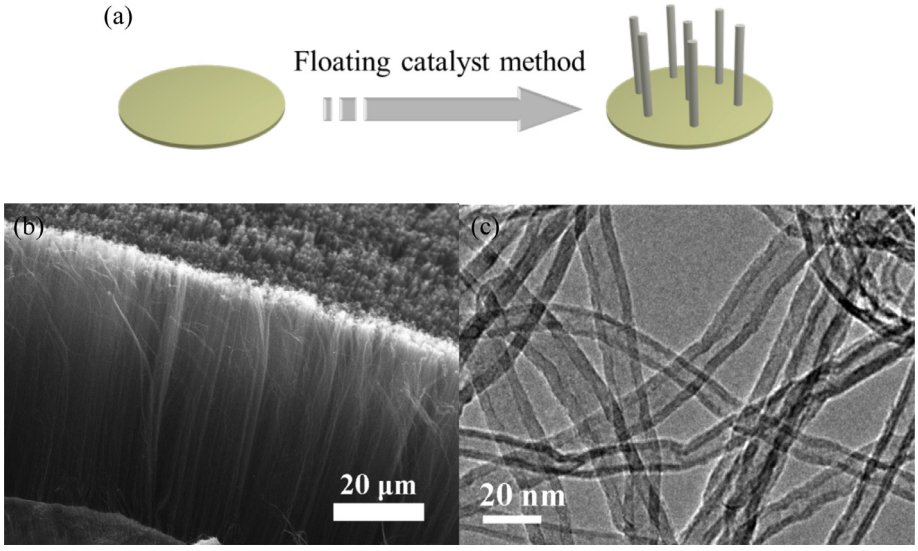

Fig. 10. (a) Schematic illustration for the growth of ACNTs over conductive substrate using one-step floating catalyst method. (b) SEM and (c) TEM images of ACNTs grown over Al foil using a floating catalyst method [182].

substrate [176]. The complicated growth process and high cost of this method limits its wide applications, although extremely long carbon nanotubes with high degree of alignment can be obtained. Metal substrates, which are used as current collectors, are not stable under certain conditions [178]. Therefore, the preparation of pure carbon based 3D electrodes has attracted considerable interest [176,179,180]. Many researchers attempt to grow ACNTs directly over graphene film. However, the unbalance surface energy between transition metal catalyst and carbon makes the directly growth of ACNTs impossible. Therefore, an alumina buffer layer is normally introduced to solve this issue [176,180].

3.1.3. One-step floating catalyst method

Ajayan and co-workers firstly reported the growth of ACNTs directly over electrically conductive Inconel 600 substrate via a one-step floating catalyst method (Fig. 10a) [158]. They believed Inconel 600 can balance the catalyst and substrate interaction, minimize surface diffusion and promote the formation of high density catalyst nanoparticles, which facilitates the formation of stable catalyst nanoparticles and result in the growth of ACNTs. These ACNTs/metal structures were then utilized to fabricate electric double-layer capacitors, which demonstrated improved performance over previously designed carbon nanotube structures. Additionally, Chang et al. reported the possibility of growth ACNTs over Al foil, which is relatively cheap, through floating catalyst method [181]. Ferrocene and acetylene were employed as a catalyst precursor and carbon source, respectively, for the growth of ACNTs via three-temperature-zone chemical vapor deposition method.

In our group, we have synthesized carbon nanostructures over different conductive substrates, including titanium [33,183], stainless steel [184], graphite [185], aluminium [32,182], copper [186] foils etc. However, high quality ACNTs can only be synthesized over titanium, stainless steel and aluminum foils which show low surface tension energy [185]. Carbon nanofibers can be obtained over graphite and copper foils. Titanium is considered as being corrosion resistant because of the formation of a titanium oxide passivation layer [187]. Therefore, it is an ideal current collector for energy storage. However, titanium experiences phase transformation at high temperatures during the growth of carbon nanotubes which makes it fragile, thus resulted in limited applications. Stainless steel is corrosion resistant and cheap, and it can be utilized as current collectors for both SCs and LIBs. Recently, high quality ACNTs have been successfully grown over stainless steel 304 using one-step floating catalyst method in our group. The ACNTs/stainless steel 3D structures were employed as both anode and cathode current collector for LIBs. Very promising results have been obtained by utilizing this 3D current collector. Aluminum foil is widely used as cathode current collector for LIBs due to its low price and density as well as high stability at high potential [188]. Well ACNTs have been obtained in our group via a one-step floating catalyst method (Fig. 10b and c) [32,33,182,185].

3.2. Coating of active materials over aligned carbon nanotubes

3.2.1. Conducting polymer

The conducting polymers, such as polyaniline, polypyrrole, and polythiophene derivatives etc., have been proposed and investigated for energy storage [18,189,190]. because the whole mass and volume can be involved in charge storage which results in extremely high specific energy [190]. Conducting polymers can be synthesized by both chemical polymerization and electrochemical polymerization. Two oxidation reactions take place simultaneously: the oxidation of the monomer and the oxidation of the polymer accompanying by the insertion of a dopant [191]. Electrochemical polymerization are preferred due to its advantage of a precise control of potential and state of charge of the resulting polymer [18].

Polyaniline can be produced by chemical or anodic oxidation of aniline monomer. It involves three states, namely pernigraniline, emeraldine and leucoemeraldine, which presents a color of blue/violet, green/blue and white/clear, respectively [183]. Polyaniline can be coated onto carbon nanotubes uniformly through chemical oxidation of aniline monomers by ammonium peroxodisulphate in the presence of carbon nanotubes in aqueous medium [192,193]. The thickness of the polyaniline layers could be effectively controlled by varying the ratio of aniline monomers and carbon nanotubes. The results indicated that the presence of carbon nanotubes with minimized defects induced the formation of a more planar conformation of polyaniline even with a high loading [193]. Previously, we reported the coating of polyaniline layers over ACNTs via chemical polymerization in the aqueous solution of aniline hydrochloride and ammonium peroxodisulphate [183]. However, the polyaniline coating is not homogeneous and a layer of polyaniline film can be observed on the top of ACNTs, as shown in Fig. 11(a). This might be attributed to that polyaniline nucleation occurs in the bulk solution which results in the deposition of polyaniline onto the top of ACNTs arrays.

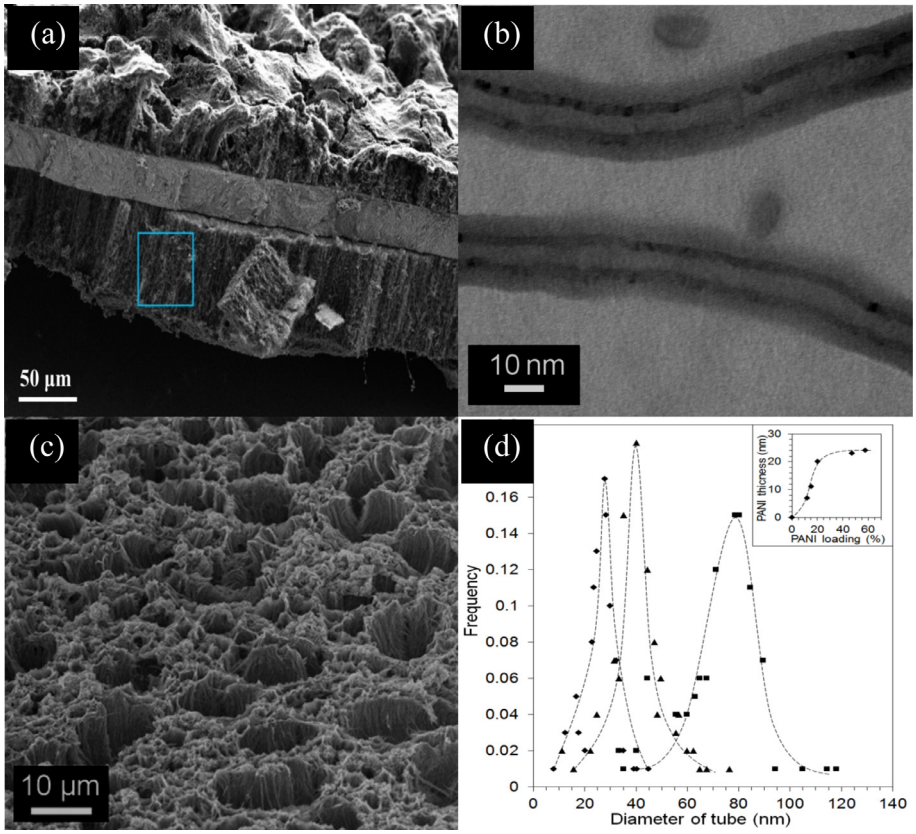

Fig. 11. SEM images of polyaniline coated ACNTs by (a) chemical polymerization [183] and (c) electrochemical polymerization [32]. (b) Image of polyaniline coated ACNTs by electrochemical polymerization [32]. Size distribution of polyaniline coated ACNTs and the dependence of polyaniline thickness on the loading [33].

Recently, we demonstrated the uniform coating of polyaniline film over the entire surface of ACNTs via cyclic voltammetry (CV) method with a sweeping rate of 50 mV/s from -0.2 V to 0.8 V (vs. Ag/AgCl) (Fig. 11b) [32,33]. The honeycomb microstructure was formed after polyaniline coating (Fig. 11c) which is totally different from the structures obtained by chemical oxidation (Fig. 11a). The thickness of the polyaniline film could be effectively controlled by tuning the polyaniline loading through the cyclic number of CV (Fig. 11d). The uniform polyaniline coated ACNTs with high specific surface area has been reported by Zhang et al. as well [194,195].

Polypyrrole and its derivatives are of great interest due to their high conductivity and stability [196]. Moreover, the simplicity of the synthetic procedures and wide availability of the initial monomers are also attractive features of polypyrrole. However, polypyrrole cannot be n-doped, and hence it has only been used as a cathode material [191]. Polypyrrole can be prepared by oxidation of the monomer either by chemical way or by electrochemical way. Hughes et al. reported the uniform coating of ACNTs with polypyrrole via electrochemical polymerization at an oxidizing potential of 0.7 V (vs. saturated calomel electrode, SCE) in aqueous electrolyte consisting of 0.5 M pyrrole and 0.5 M KCl [197]. Polypyrrole formed a continues layer over the entire ACNTs surface and the channel formed between nanotubes could be preserved when the polymerization charges reached up to 40 C/cm^2 [197]. Additionally, Ren et al. also reported the electrochemical synthesis of uniform polypyrrole films over each nanotubes of ACNTs arrays [198]. The polypyrrole films were synthesized potentiodynamically by scanning between 0 and 0.8 V vs SCE at 5 mV/s in 0.0174 M pyrrole and 0.1 M $LiClO_4$ aqueous solution. Before polypyrrole synthesis, ACNTs were pretreated with nitric acid to improve their hydrophilicity which enables uniform polypyrrole coating. Besides, He et al. demonstrated the coating of polypyrrole layers over ACNTs via electropolymerization as well [199]. Electropolymerization was conducted utilizing CV by scanning between 0 and 1.0 V (vs. Ag/AgCl) in pyrrole and $LiClO_4$ aqueous solution. However, some polypyrrole nanoparticles have been observed on the top of ACNTs arrays at high loading.

Poly(3,4-ethylenedioxythiophene) belongs to the derivatives of polythiophene which is stable in air and moisture. It is featured by a high electrical conductivity in the p-doped state, good thermal and chemical stability and fast electrochemical switching [200]. Polymerization of 3,4-ethylenedioxythiophene has been carried out in aprotic medium such as acetonitrile as oxidant due to its limited solubility in aqueous solution [190,200]. Poly(3,4-ethylenedioxythiophene) coating over carbon nanotubes have been prepared by Frackowiak el al. through chemical and electrochemical polymerization [200]. Additionally, Wallace et al. reported the coating of poly(3,4-ethylenedioxythiophene) over ACNTs by chemical vapor phase polymerization using ferric *p*-toluenesulfonate as oxidant [201].

3.2.2. Transition metal oxides

Transition metal oxides are of great interest for energy storage due to their fast Faradaic redox reactions based charge storage mechanism for pseudocapacitors and their capability of storing lithium ions by the conversion mechanism for LIBs [202]. MnO_x and FeO_x are promising electrode materials for SCs [150,203–206] and LIBs [92,100,167,186,207–211] owing to their low cost, environmental friendliness, high specific energy, and natural abundance [182]. However, their potential applications in commercial energy storages are limited because of their poor electrical conductivity resulted poor performance. Therefore, the incorporation of highly conductive carbon nanotubes into MnO_x and FeO_x would be an effective route to improve their conductivity and thus electrochemical performance.

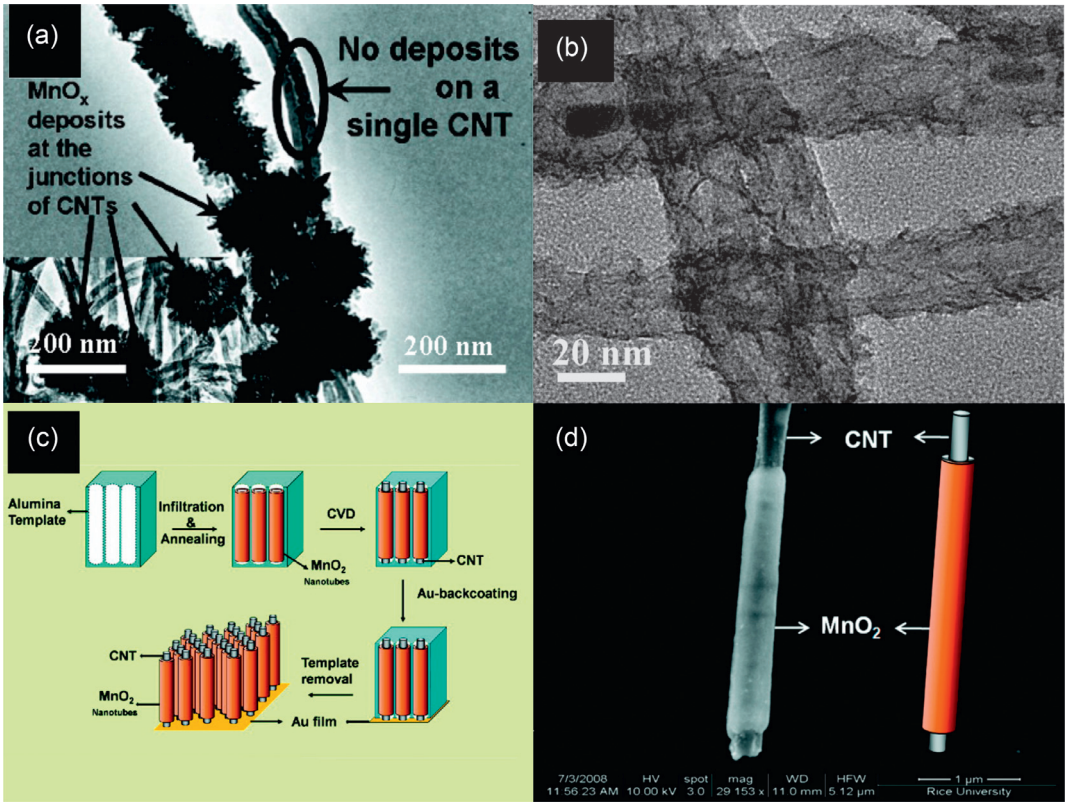

Fig. 12. TEM image of MnO_x coated ACNTs through (a) electrodeposition [147] and (b) reduction of potassium permanganate [182]. (c) Schematic diagram showing the fabrication of MnO_2/ACNTs inside anodized aluminium oxide template using a combination of simple vacuum infiltration and chemical vapor deposition techniques [167]. (d) SEM image and a schematic representation of a single coaxial nanotube [167].

MnO_x can be loaded over the surface of ACNTs either through electrodeposition or the reduction of potassium permanganate. Large particles are generally obtained via electrodeposition (Fig. 12a) and moreover the coating is not uniform which results in the inefficient use of carbon nanotubes [147] However, ultrathin film can be coated over ACNTs *via* reduction of potassium permanganate by carbon nanotubes (Fig. 12b) [182]. Zhang et al. reported the coating of MnO_x over ACNTs via electrodeposition [147]. MnO_x was electrodeposited on ACNTs using potentiodynamic method in the potential range from 0 to 1.2 V (vs saturated calomel electrode) at sweep rate of 100 mV/s for 100 cycles in 1 M Na_2SO_4 and 0.5 M $MnSO_4$ aqueous electrolyte. MnO_x particles which are around 150 nm in diameter are well dispersed over ACNTs. MnO_x particle is composed of hundreds of surfboard-shaped nanosheets, and the nanosheets of each individual particle originate from the same core, forming a dandelion-like flower. Moreover, Chen et al. claimed the coating of 12 nm MnO_2 uniform film on the whole surface of ACNTs by electrochemically induced deposition method followed by calcination in air [212]. The deposition of manganese hydroxide was performed by the galvanostatic method at a current density of 20mA/cm^2 using 0.1 Na_2SO_4 and 5 g/L polyglycol as electrolyte and 0.1 M $Mn(CH_3COO)_2$ and 0.1 M Na_2SO_4 as supplied solution. However, manganese hydroxide only deposited on the top of ACNTs through direct electrochemical deposition. They deduced the gradual diffusion of Mn^{2+} to the surface of ACNTs is critical for the uniform coating of manganese hydroxide. Recently, we developed a method for the uniform coating of MnO_x film on ACNTs through the spontaneous reduction of potassium permanganate by carbon. The spontaneous deposition of MnO_x over ACNTs is attributed to the difference in the reduction potential between carbon nanotubes and MnO_4^- [182]. Untralthin and uniform MnO_x film can be coated on the surface of ACNTs via this solution based method. Additionally, Ajayan et al. demonstrated the preparation of MnO_2 coated ACNTs using anodized aluminium oxide as template [167]. MnO_2 nanotubes were prepared firstly by infiltration of $MnNO_3$ solution into anodized aluminium oxide template followed by annealing at high temperature. Then carbon nanotubes were grown in the internal surface of MnO_2 nanotubes through chemical vapor deposition. Finally, MnO_2 coated ACNTs were obtained by dissolving alumina templates in 3 M NaOH aqueous solution (Fig. 12c and d).

Recently, FeO_x was grown on ACNTs in our group via spontaneous reduction of potassium ferrate by carbon nanotubes [184]. Potassium ferrate is a powerful oxidant with a reduction potential of 0.72 V in basic medium [213]. One challenge of FeO_x coating over carbon nanotubes through this method is that potassium ferrate solution is only stable in a concentrated alkaline solution. Another challenge is that potassium ferrate solution has very high viscosity [214]. Therefore, a precursor solution of 25 mM K_2FeO_4 in 9 M KOH was employed to provide the optimal balance between stability of the ferrate precursor in solution and its reactivity toward the oxidation of carbon nanotubes and reduce the viscosity [206]. The as-synthesized ACNTs were pretreated with oxygen plasma to improve the hydrophilicity. After immersion the pretreated ACNTs in 25 mM K_2FeO_4 in 9 M KOH aqueous solution for 12 h, well dispersed FeO_x nanoparticles can be coated over ACNTs (Fig. 13).

3.2.3. Spinel and orthosilicates

$LiMn_2O_4$ spinel has attracted great interest due to its favorable charge storage capacity, high ionic conductivity, low cost, and environmental friendliness [103]. In general, the electrochemical performance of $LiMn_2O_4$ is strongly related to its phase purity, crystallinity, particle size, and morphology, which are correlated to the materials synthesis [215]. $LiMn_2O_4$ can be fabricated by solid state reaction and soft chemistry methods, such as sol gel, spray dry,

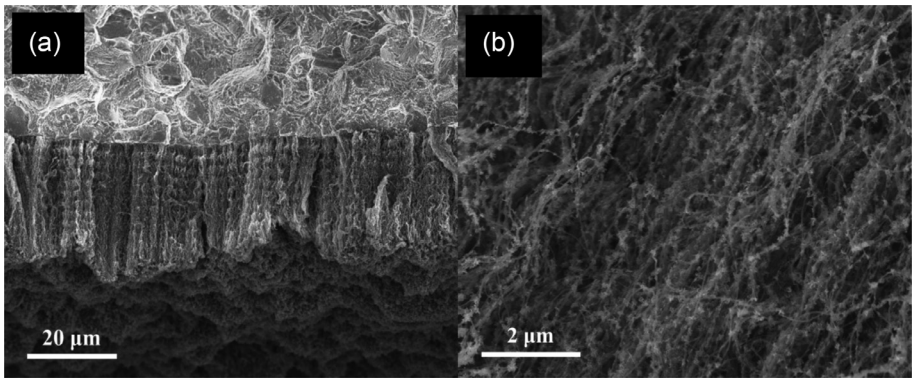

Fig. 13. SEM images of FeO_x coated ACNTs at different resolutions [184].

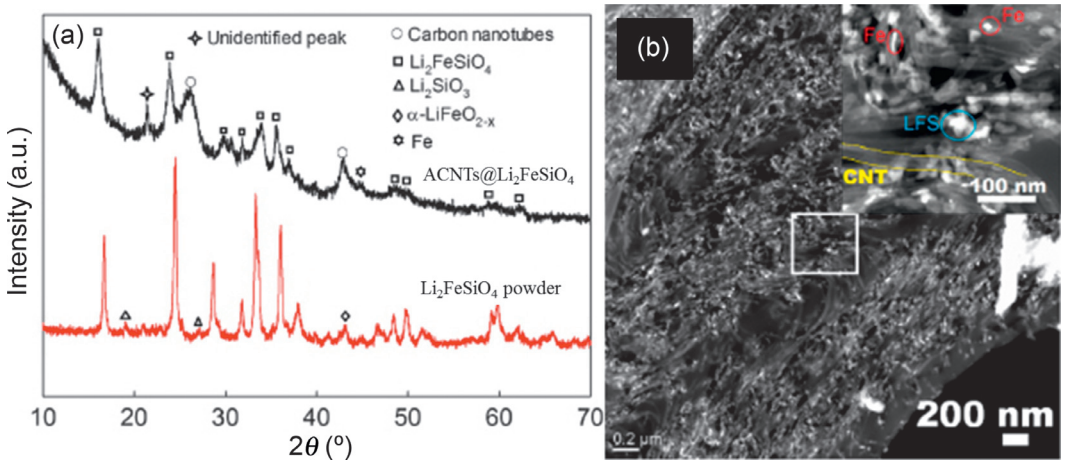

Fig. 14. (a) XRD patterns of ACNTs@Li_2FeSiO_4 and Li_2FeSiO_4 powder. (b) Low angle annular dark field (LAADF) scanning TEM image taken from the interface part of the ACNTs@Li_2FeSiO_4 nanocomposite adjacent to the Al substrate [218].

melt impregnation. However, these methods suffer from high temperature annealing process in air which could destroy ACNTs. Recently, hydrothermal method was employed for the deposition of $LiMn_2O_4$ over ACNTs in our group. MnO_x was loaded over ACNTs firstly via spontaneous reduction of potassium permanganate. Then MnO_x was transferred to $LiMn_2O_4$ through on-step hydrothermal reaction with LiOH, which serves as lithium source and reducing agent.

Orthosilicate Li_2MSiO_4 (M = Fe, Mn, etc.) are the most attractive cathode materials for LIBs due to their potential ability to allow two electron exchange per formula unit resulting in lithium ion storage capacity of ≥300 mAh/g [67,216]. Additionally, it is characterized by the high safety arising from the strong Si–O covalent bond, environmental friendliness and low cost [217]. However, orthosilicate cathodes normally only deliver a reversible capacity of about 160 mAh/g which results from their extremely poor electronic and ionic conductivities [217]. The coating of orthosilicate thin film over ACNTs would be a promising solution to enhance the electronic conductivity and reduce the lithium ion diffusion distance. In one of our recent work, Li_2FeSiO_4 and Li_2MnSiO_4 were coated over ACNTs via sol gel method [218]. A Li-Fe/Mn-Si-PVA solution was prepared by a wet chemical method. Polyvinyl alcohol was employed as complexing and reducing agents during the carbon thermal reaction. The prepared solution was applied drop-wise on the top of ACNTs. This process was followed by aging at room temperature for 10 h to obtain a gel-coated composite, and annealing in argon at 600°C for 10 h to obtain the final Li_2FeSiO_4 coated ACNTs. The successful synthesis of Li_2FeSiO_4 was confirmed by XRD and TEM (Fig. 14).

3.2.4. Other active materials

As described above, one effective way to improve the specific energy of LIBs is to significantly increase the specific capacity of electrode materials. The commercial LIBs with $LiCoO_2$ and graphite as electrode materials can deliver a specific eneryg of about 400 Wh/kg. A new pair of electrode materials using lithium doped sulfur and silicon as cathode and anode, respectively, can increase the specific eneryg up to 1550 Wh/kg [219]. This can be attributed to the extremely high specific capacities of sulfur and silicon (Table 2), although the operation voltage is moderate.

The low discharge potential and high theoretical specific capacity of silicon have raised significant interest on silicon based anodes for LIBs [220]. However, during lithiation, lithium/silicon alloying yields very high volume expansion, up to 300%, which induces high mechanical stress leading to significant capacity fading [152]. The first cycle irreversible loss of silicon is another issue needs to be solved before its wide application. The coating of silicon over ACNTs would be an ideal way to address these problems. The large space between carbon nanotubes can accommodate the volume change. In addition, the carbon nanotube arrays prompt favorable lithium ions and electrons transport which results in the reduction in first cycle irreversible loss [221]. The theoretical capacity of sulfur is 1675 mAh/g which is significantly higher compared with metal oxide and phosphate [70]. However, the poor electrical conductivity of sulfur results in only low utilization of the active material. Therefore, the coating of sulfur over ACNTs would be an efficient way to improve its conductivity. Kaskel et al. reported the preparation of sulfur coated ACNTs composites via infiltration which is achieved from sulfur solutions in toluene [69].

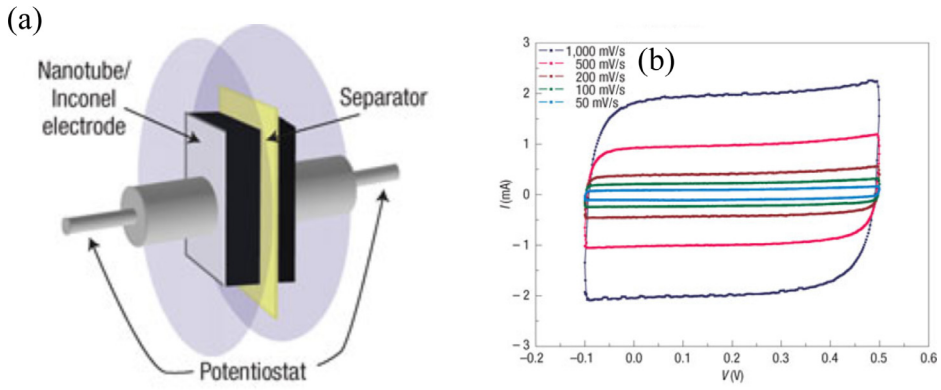

Fig. 15. (a) The experimental arrangement used to fabricate and measure the capacitive properties of the ACNTs/Inconel electrodes. (b) Cyclic voltammograms measured for a particular SCs device at scan rates ranging from 50 mV/s to 1000 mV/s [158].

4. Applications in electrical energy storages

4.1. Supercapacitors

4.1.1. Aligned carbon nanotubes

ACNTs have been prepared over conductive substrates through either template method [159], transfer from non-conductive substrates[169,170,222] or growth over conductive substrates with [177] or without a buffer layers [158,166,223] as electrodes for SCs.

The capacitive behavior of ACNTs was first reported by Martin et al. through CV in sulfuric acid electrolyte [159]. Afterward, Ajayan and co-workers reported the direct growth of ACNTs over Inconel 600 for SCs, which exhibited a specific capacitance of 18 F/g in 6 M KOH (Fig. 15) [158]. The CV curves exhibited a rectangular and symmetric shape even at a high scan rate of 1000 mV/s (Fig. 15b), suggesting good rate performance and low contact resistance between the carbon nanotubes and Inconel [158]. Later, Ajayan et al. embedded the ACNTs into cellulose, which was used as spacer, to fabricate an ultrathin and flexible electrode [224]. ACNTs showed capacitances of 36 and 22 F/g in 6 M KOH and an ionic liquid electrolyte, respectively. The lower specific capacitance with ionic liquid electrolyte relative to KOH electrolyte can be attributed to the lower dielectric constant and ionic mobility of the former electrolyte. Very recently, his group reported hybrid nanostructured electrodes consisting of ACNTs on highly porous carbon nanocups which were synthesized by a combination of anodization and chemical vapor deposition method [166]. The hybrid carbon electrodes showed a relatively high specific capacitance of 45 F/g in 1 M $LiPF_6$ in ethylene carbonate and dimethyl carbonate (1:1, v/v) due to their high specific surface area (1340 m^2/g).

Additionally, Zhang and co-workers also did a series of great works on the applications of ACNTs as electrodes for SCs [146,169,177,225,226]. In the beginning, they prepared 800 μm long ACNTs electrodes by transferring them from silica to nickel foam [169]. The obtained electrode showed a moderate specific capacitance of 14.1 F/g in 7 M KOH but excellent rate capability. Later they investigated the capacitive behavior of 500 μm long ACNTs in Et_4NPF_6/propylene carbonate electrolyte and a specific capacitance of 24.5 F/g was obtained [225]. They continued their work on ACNTs for high temperature SCs using ionic liquid electrolyte [226]. ACNTs can achieve a specific capacitance of 27 F/g, show excellent rate capability, and maintain a long cyclic stability at 60°C. In 2008, they started to grow ACNTs directly on conductive substrates, such as glassy carbon and Ta foil, with a Al_2O_3 buffer layer [177]. The specific capacitances of ACNTs on glassy carbon and Ta are 27 and 28 F/g, respectively, at a current density of 0.5 A/g in 1 M H_2SO_4, which are comparable with the specific capacitance of mm-long ACNTs. However, the capacity retention of ACNTs grown directly on conductive substrates is more than 50% at a high current density of 100 A/g, indicating excellent rate capability which is much better than that of the ACNTs electrodes prepared by transfer techniques.

Moreover, Shah et al. reported the fabrication of SCs with ACNTs grown directly on conductive substrates as well [223]. The obtained SCs show very small equivalent series resistances down to less than 1 Ω. The specific capacitance of ACNTs ranged from 10.75 to 21.57 F/g depending on the length. Besides, Ishikawa and co-workers prepared ACNTs over aluminum foil by a transfer procedure for SCs [170]. ACNTs exhibit a specific capacitance of 10–15 F/g even at an extremely high current density of 200 A/g. Recently, Dai's group reported the effect of plasma etching on the capacitive behavior of ACNTs in ionic liquid electrolyte [222]. They observed plasma etching can enhance the capacitive behavior of ACNTs by opening the end tips of nanotubes and introducing defects and oxygenated functionalization to the surface of nanotubes.

4.1.2. Conducting polymers

As presented above, the specific capacitance of ACNTs contributed from electric double-layer alone is very limited. Therefore, the introduction of other materials with high pseudocapacitance is necessary to improve the specific energy of resulted SCs. Electrically conducting polymer is an option due to its high theoretical specific capacitance (Table 1).

Conducting polymers are rendered conductive through a conjugated bond system along the polymer backbone [191]. They must capture and release ions to maintain electroneutrality during electrochemical oxidation and reduction which is known as doping and un-doping. The doping is an ion insertion process which increases the redox state and electronic conductivity of the conducting polymer [18]. Conducting polymers can be n-doped with cations when reduced and p-doped with anions when oxidized. The charging processes of these two can be simplified expressed as follows [191]:

$$Cp \rightarrow Cp^{n+}(A^-)_n + ne^- \quad (p-doping)$$

$$Cp + ne^- \rightarrow (C^+)_n\, Cp^{n-} \quad (n-doping)$$

The discharging processes are the reverse of the above equations.

The uniform coating of polypyrrole over ACNTs via electrochemical polymerization was first reported by Ren and co-workers in 2001 [198]. The redox performance of the polypyrrole coated ACNTs in 0.1 M $LiClO_4$ aqueous solution was significantly improved due to the high accessible surface area of the carbon nanotubes in the aligned arrays. One year later Hughes et al. also investigated the capacitive behavior of polypyrrole coated ACNTs [197]. A continuous polypyrrole layer is coated over each carbon nanotube in the aligned arrays through electrochemical polymerization. They observed the ionic resistance of polypyrrole film in 0.5 M KCl is much higher compared with polypyrrole coated ACNTs due to the high electrolyte accessibility of later one through their regular channels. In their work, a

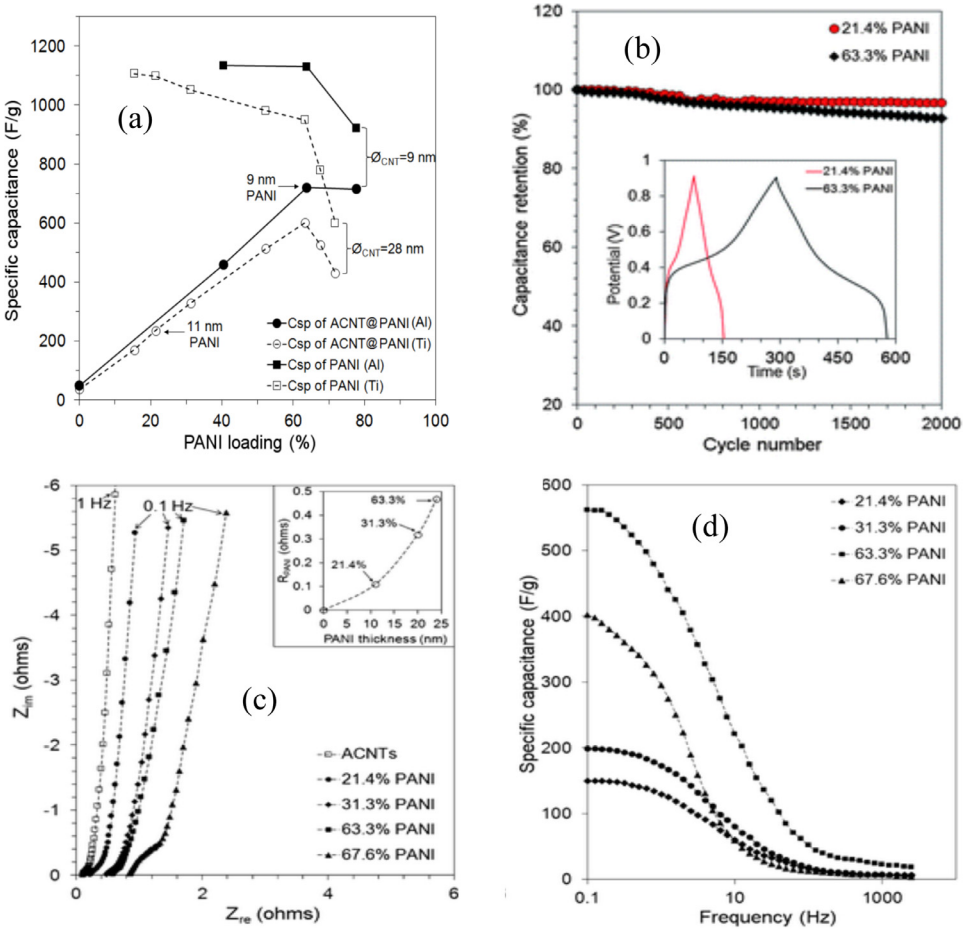

Fig. 16. (a) Comparison of specific capacitance based on the mass of the composites and polyaniline alone between the composites on household Al and Ti foil [32]. (b) Cyclic stability of the composites with different polyaniline loading at 2.0 A/g [33]. (c) Nyquist plot and the inserted plot for the resistance of polyaniline layer versus polyaniline thickness [33]. (d) The dependence of specific capacitance of the composites on the frequency [33].

charge storage capacitance as high as 2.55 F/cm^2 has been achieved [197]. In addition, Zhang and co-workers reported the polyaniline coated ACNTs exhibited a high specific capacitance of 1030 F/g, superior rate capability with 95% capacitance retention at 118 A/g, and high stability with 94.5% capacity retention after 5000 cycles [195]. They ascribed this excellent capacitive performance of polyaniline coated ACNTs to their hierarchical porous structure, large surface area, and superior conductivity. Besides, they also investigated the influence of microstructure on the capacitive performance of polyaniline coated ACNTs [194]. It was found the specific capacitances of polyaniline coated ACNTs composites are strongly influenced by their microstructure which is determined by the polyaniline loading.

Recently, we reported a systematic study on the relationship between the microstructures of the polyaniline coated ACNTs on Ti foil and the electrochemical performances as electrodes for SCs [33]. The objective is to approach the theoretical specific capacitance, heighten rate capability, and achieve good cyclic stability by the rational design of the electrode materials. The thickness of the polyaniline film coated on each nanotube was concluded the most important parameter, which was optimized to achieve the specific capacitance of polyaniline close to the theoretic value (1267 F/g) [33]. Afterward, we applied this conclusion to ACNTs grown on household Al foil which have thinner diameter and thereby higher specific surface area compared with those grown on Ta foil, aiming to increase the polyaniline loading but maintain the film thickness [32].

A series of polyaniline films with different thicknesses were coated on ACNTs by electrochemical polymerization to investigate its effects on the electrochemical performances in terms of specific capacitance and cyclic stability [33]. The dependence of the capacitance (based on the weight of polyaniline alone) on the polyaniline loading can be divided into three regions (Fig. 16a, Ta foil as substrates). The capacitance is approaching the theoretical value of polyaniline and keeps almost constant up to approximately 21.4 wt% polyaniline loading, which is corresponding to 11 nm polyaniline films [33]. This implies that all the active groups in the polyaniline chains can participate in the redox reaction and contribute to its intrinsic capacitance as long as the film is thinner than 11 nm. The specific capacitance of polyaniline is followed by a mild decrease until the loading reaches 63.3 wt%, thereby indicating a slightly lower specific capacitance of polyaniline with a larger thickness up to 24 nm [33]. A primary reason for this might be the insufficient usage of the inner part of the polyaniline film. The specific capacitance decreases rapidly with a further increase in polyaniline loading because polyaniline has filled the space between nanotubes and start to grow on the top of the arrays which block the fast electrolyte transfer in the arrays. These conclusions were applied to the ACNTs grown on Al foil. Fig. 16(a) clearly shows the improvement in the specific capacitance of the composite on the Al foil comparing with that on the Ti foil due to a smaller diameter of ACNTs [32]. The increase in the maximum capacitance is mainly a result of reduced thickness of the polyaniline film on the ACNTs@PANI/Al foils comparing with one on the Ti foils at the identical polyaniline loading. After 2000 cycles at 2 A/g, the capacitance

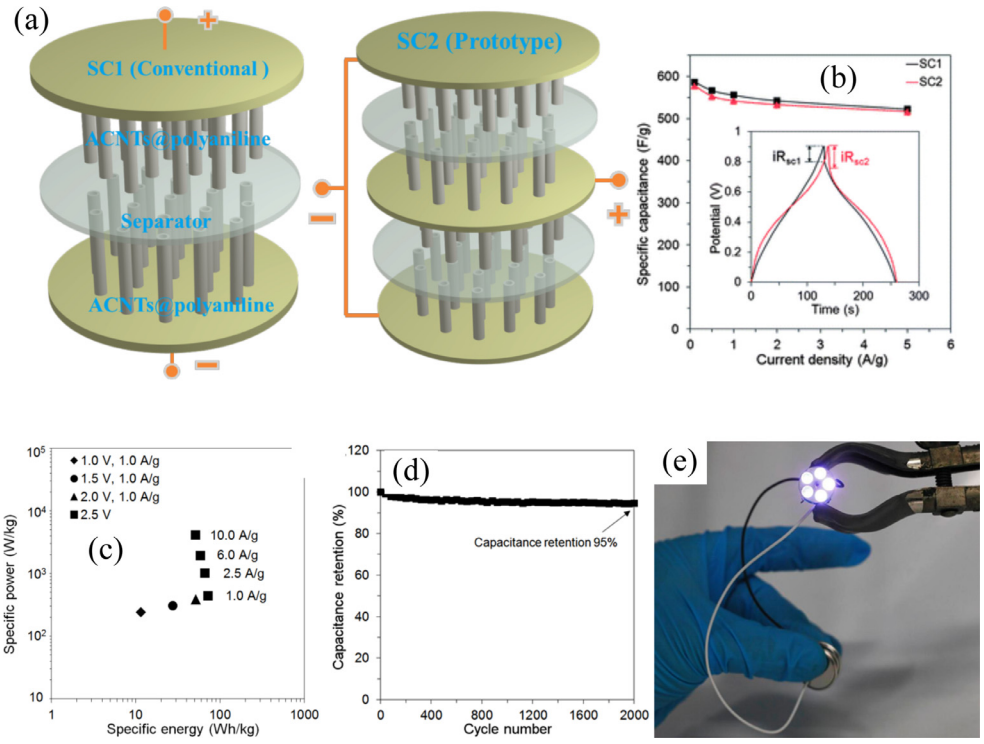

Fig. 17. (a) Schematic illustrations of a conventional two-plate supercapacitor (SC1) and a prototype three-layer supercapacitor (SC2) [33]. (b) Discharge specific capacitance vs current density and inserted plots of galvanostatic charge–discharge of SC1 and SC2 at 2.0 A/g from 0 to 0.9 V [33]. (c) Ragone plot for the average specific power and specific energy of the active materials [32]. (d) Cycling stability of the coin-cell supercapacitor charged and discharged at 1.0 A/g from 0 to 2.5 V for 2000 cycles at room temperature [32]. (e) Digital photograph of five light-emitting diodes (LEDs) in parallel, powered by two coin-cell SCs in series [32].

retention of the composites containing 63.3% and 21.4% of polyaniline was 92.9% and 96.7%, respectively [33]. Therefore, the composite with thinner polyaniline layer on the ACNTs shows higher cyclic stability than the one with thicker polyaniline layer (Fig. 16b). This can be attributed to the large strain during charge and discharge which causes the break of polyaniline from ACNTs.

The electrochemical impedance spectra were analyzed to decouple the effects of surface reactions and external and internal ionic diffusion on the electrochemical performance [33]. The internal resistance of ACNTs on Ti foils is only 0.11 Ω, which is contributed by the low resistance of carbon nanotubes and the low contact resistance between carbon nanotubes and Ti foil [33]. The resistance difference between the composite and carbon nanotubes alone is the resistance of the polyaniline layer which is shown in the inset of Fig. 16(c) as a function of the film thickness [33]. The resistance of the polyaniline (R_{PANI}) increases slightly up to 11 nm polyaniline film, which increases rapidly as the polyaniline becomes thicker. The low internal resistance is attributed to the short conductive path and reduced contact resistance provided by ACNTs grown on the current collector [33]. The Nyquist plot shows an existing loop in the high frequency range which is related to the surface charge transfer process. A very small loop for the composites with relatively low polyaniline loadings indicated a low surface charge transfer resistance. The resistance of the ionic diffusion is proportional to the slope of the impedance curves at the low frequency range. The figure suggested that the slope slightly decreases with an increasing polyaniline thickness, thereby indicating an increase in ionic diffusion resistance. In Fig. 16(d), the relatively flat region found in the composites with polyaniline loading less than 63.3 wt% indicates that ions can penetrate the entire polyaniline layer at a very low frequency, and the redox reaction takes place on all the active sites. However, much lower capacitances were found when the polyaniline loading increases from 63.3 wt% to 67.6 wt%. This might be because the loss of the regular pore structure or the complete blockage of the pore in the composite material reduces the ionic transfer rate to a great extent at high polyaniline loading [33].

In addition to optimizing the electrode materials, the configuration of the device is another important factor to get high specific energy and specific power of the whole SCs [33]. The mass fraction of the conductive substrate plays an important role in the performance of the entire device. The strategy to reduce the mass fraction of the substrate in the entire cell is to increase the polyaniline loading, grow ACNTs on both sides of the substrate and use lighter substrates, such as Al foils [33]. A prototype SCs (SC2) with a three-layer configuration was built (Fig. 17a), where the electrode with two-sided ACNTs@(63.3 wt% polyaniline) in the middle was sandwiched between two one-sided ACNTs@ polyaniline electrodes [33]. A conventional two-plate supercapacitor (SC1) was assembled and examined as a reference for a comparison. The specific capacitances of SC1 and SC2 are 542 F/g and 533 F/g, respectively, based on weight of polyaniline and ACNTs at 2.0 A/g which are very similar [33]. However, the specific capacitances of SC1 and SC2 are 9.0 F/g and 12.3 F/g, respectively, based on the weight of polyaniline, ACNTs and Ti foil at 2.0 A/g. The 36.7% increase in the specific capacitance of the SC2 can be attributed to the reduced mass fraction of the Ti foil in the entire cell [33]. The internal resistances of SC1 and SC2 devices are 2.8 Ω and 1.9 Ω, respectively. The internal resistance of SC2 is lower than that of SC1 because the parallel configuration of SC2 reduces the total internal resistance [33]. This results in a higher maximum specific power of SC2 (274 W/kg) than SC1 (267 W/kg) based on the mass of the entire device.

In order to operate the device in a wider voltage window, which can significantly increase the specific energy according to Equation (1), organic electrolyte was employed. A high specific energy of 72.4 Wh/kg has been achieved at an average specific power of 430.8 W/kg using the organic electrolyte which can operate at 2.5 V (Fig. 17c) [32]. The electrode material also shows good cyclic stability in organic

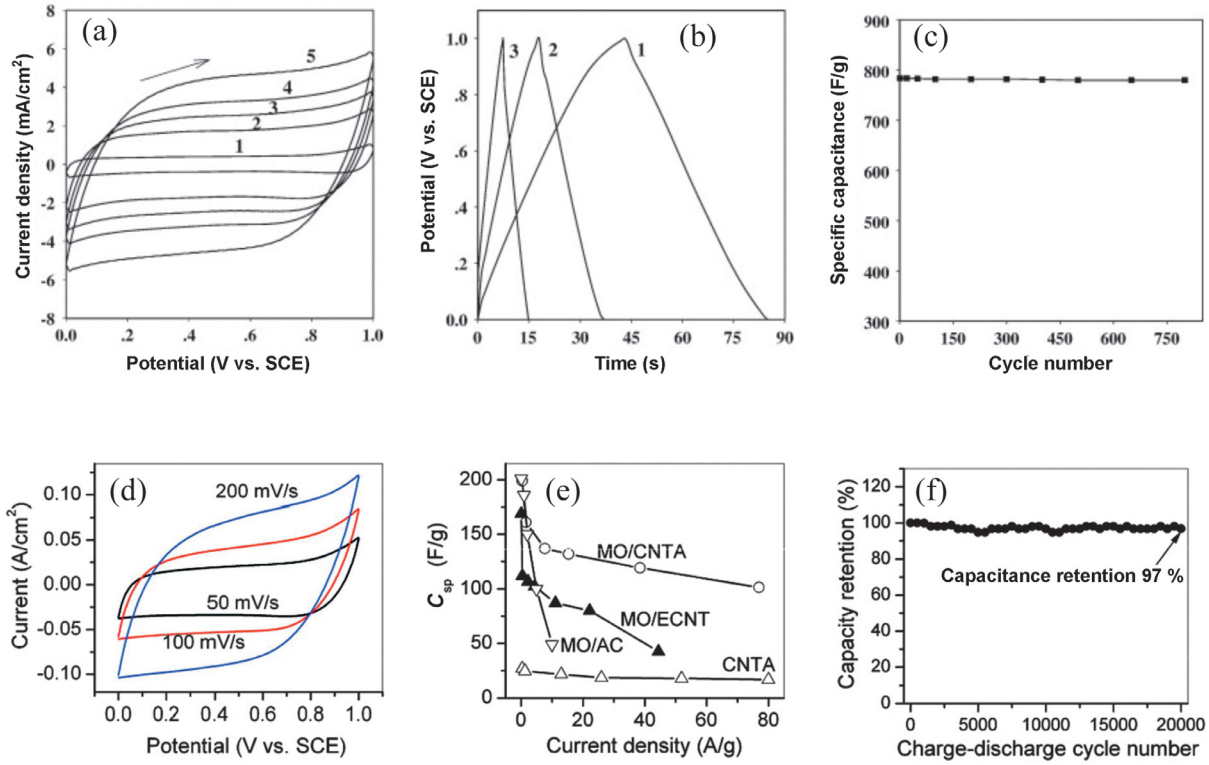

Fig. 18. (a) Cyclic voltammograms, (b) chronopotentiograms, and (c) cyclic stability of the ACNTs@γ-MnO_2 electrode in 0.1 M Na_2SO_4 aqueous solution [212]. (d) Cyclic voltammograms, (e) specific capacitance vs discharge current density, and (f) cyclic stability of ACNTs@MnO_x [147].

electrolyte. The coin-cell was charge and discharged for 2000 cycles from 0 to 2.5 V at 1.0 A/g and a reduction of ~5% in the capacitance was found after 2000 cycles (Fig. 17d) [32]. Two coin-cell SCs made from the same electrode materials were connected in a series combination and charged to 5 V to illuminate the LEDs with an input power of around 150 mW (Fig. 17e) [32]. The LEDs illuminated for nearly 15 s with the brightest light at the beginning and gradually dimmed afterward.

4.1.3. Metal oxides

Chen *et al.* reported the capacitive behavior of MnO_2 coated ACNTs which were prepared by electrochemically induced deposition [212]. Cyclic voltammograms exhibit well symmetric and rectangular-like shape, even at a high scan rate of 150 mV/s (Fig. 18 curve 5), suggesting the high power characteristics of the electrode. It can be seen that all curves are highly linear and symmetrical. This implies that the electrode has excellent electrochemical reversibility and charge–discharge properties. The specific capacitance of the ACNTs@γ-MnO_2 are 784, 765 and 707 F/g at current densities of 1, 2 and 5 mA/cm^2, respectively, based on γ-MnO_2 (Fig. 18b). Such a high specific capacitance indicates that γ-MnO_2 has very high dispersibility and usability in the ACNTs@γ-MnO_2 electrode. The good power characteristic and high specific capacitance indicate that the 3D porous structure of the ACNTs@γ-MnO_2 electrode is of great benefit to the fast penetration of protons and/or cations into the whole electrode matrix. The ACNTs@γ-MnO_2 electrode displays excellent long-term cyclic stability as well, only 0.5% decrease of the specific capacitance is observed after 800 cycles (Fig. 18c).

Zhang et al. reported the growth of MnO_x nanoflowers on ACNTs by electrodeposition for SCs [147]. The CV curve of the ACNTs@MnO_x composite shows rectangular shape at a high scan rate of 200 mV/s (Fig. 18d), indicating highly capacitive nature with good ion response. The ACNTs@MnO_x composite delivers a specific capacitance of 199 F/g (Fig. 18e) at low current density, which is much higher than the capacitance of the original ACNTs substrate (27 F/g). Surprisingly, this composite still retains 101 F/g (50.8% retention) at a current density of as high as 77 A/g, indicating that such high capacitance can be maintained under very high power operation. This is one of the best reported rate capabilities for manganese oxide composites. The electrochemical stability of the composite electrode was examined by charge–discharge cycling at a current of 5 mA. The capacity loss after 20,000 consecutive cycles is only 3%, indicative of long-term electrochemical stability [147].

4.2. Lithium ion batteries

4.2.1. Cathode

4.2.1.1. Manganese oxide. Manganese oxide (MnO_x) can accommodate one lithium per manganese oxide unit which results in a high specific capacity of 308 mAh/g, in addition to its low cost, environmental friendliness and natural abundance. Therefore, MnO_x was selected as the lithium intercalation host coated on ACNTs for LIBs in our previous work aiming to achieve high specific capacity, good cyclic stability and high rate capability [182].

A high discharge capacity of 308 mAh/g was obtained for the as-prepared MnO_x (ACNTs@MnO_x/Al), which achieves the theoretical capacity of MnO_2 (Fig. 19a) [182]. The high discharge capacity can be attributed to the MnO_x thin film which enables the entire active layer electrochemically accessible and active. However, the discharge capacity decreases to 245 mAh/g after annealing at 200°C for 12 h (ACNTs@MnO_x/Al-200) due to the partially collapse of the layered structure, which reduces accessibility of lithium ions to the active sites [182]. The discharge capacity decreases dramatically to 155 mAh/g after annealing at 300°C for 12 h (ACNTs@MnO_x/Al-300) resulting from the partial reduction of the layered manganese oxide into Mn_3O_4 [182]. Although ACNTs@MnO_x/Al exhibits high initial capacity, it suffers from serious capacity fading (Fig. 19b). The initial capacity decreases and cyclic stability improves concurrently

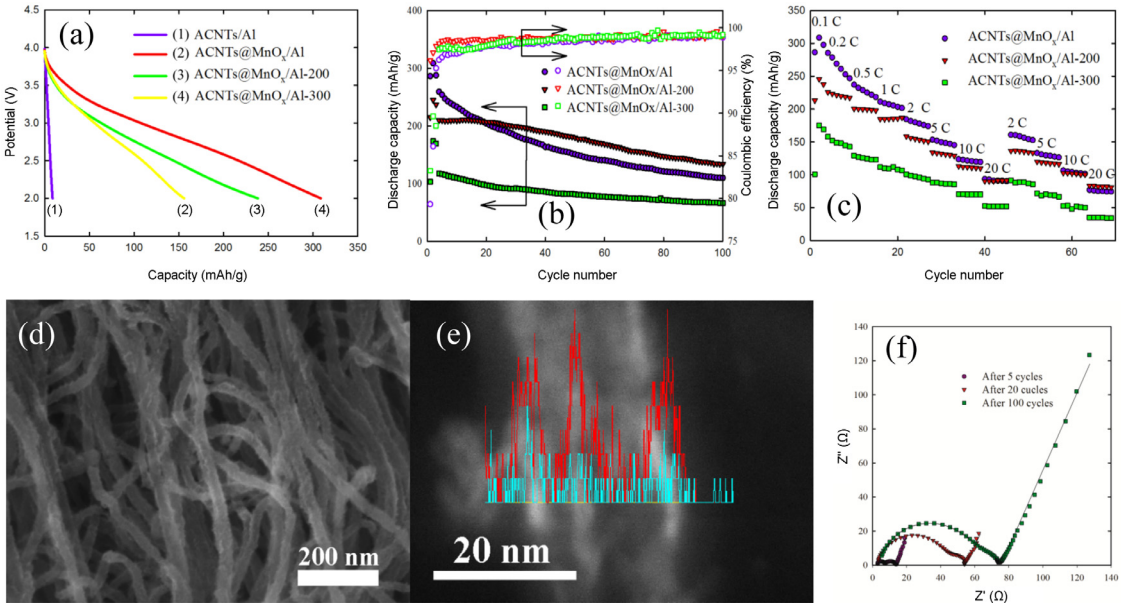

Fig. 19. (a) Discharge voltage profiles of MnO_x between 2.0 and 4.0 V vs Li^+/Li at 0.1 C. (b) Cyclic stability of MnO_x between 2.0 and 4.0 V vs Li^+/Li at 0.1 C for the first 3 cycles and 1 C for the following cycles. (c) Rate capability of MnO_x between 2.0 and 4.0 V vs Li^+/Li. (d) SEM image and (e) EDS line scanning of ACNTs@MnO_x/Al after 100 cycles. Manganese signal is in red and fluorine signal is in blue. (f) Nyquist plots of ACNTs@MnO_x/Al after various cycles at depth of discharge (DOD)=40% [182].

with increasing annealing temperature. It results in a high capacity of 133 mAh/g after 100 cycles for ACNTs@MnO_x/Al-200 [182]. The Coulombic efficiency of ACNTs@MnO_x/Al-200 is higher compared with ACNTs@MnO_x/Al in the first 40 cycles, indicating less side reactions after annealing which resulted in the improved cyclic stability (Fig. 19b). Additionally, ACNTs@MnO_x/Al and ACNTs@MnO_x/Al-200 can deliver a discharge capacity of about 95 mAh/g at a high current rate of 20 C (Fig. 19c). The excellent rate capability of the obtained MnO_x is likely due to the novel 3D current collector and MnO_x thin film, which reduces the diffusion resistance of lithium ions in the electrolyte and the shortens diffusion distance of lithium ions in the active materials. These results fully confirm the principles of rational electrode design discussed in Section 2 that ACNTs based thin film electrode can achieve high specific capacity and rate capability simultaneously due to its novel 3D nanoarchitecture.

The capacity fading of MnO_x might be resulted from Jahn–Teller distortion, phase transformations, dissolution of Mn^{2+} into the electrolyte, or others [182]. Jahn–Teller distortion, which is driven by the localized high spin $3d^4$ configuration of Mn^{3+} [227], could be excluded from the main mechanism of capacity fading directly due to the low crystallinity feature of obtained MnO_x. The discharge voltage profiles of MnO_x after 100 cycles are very similar to the fresh sample, indicating phase transformation is not the primary reason for capacity fading. Mn^{2+} dissolution can be excluded as well according to the EDS result of cycled lithium foil that Mn was not detected. The SEM images of cycled ACNTs@MnO_x/Al (Fig. 19d) shows that the MnO_x thin film was preserved very well after extended cycles [182]. Therefore, the thin MnO_x layers appear elastic enough to avoid deformation of the active layers. It clearly demonstrates the advantage of the thin film which can tolerate a large strain caused by a large volume expansion and shrinking during operation. The EDS line scanning indicated the existence of F but not P on the cycled MnO_x film (Fig. 19e), which seems to form a very thin film on the surface of the MnO_x layer. Fig. 19(f) shows the Nyquist plots of ACNTs@MnO_x/Al at DOD=40% after different cycles. The resistances corresponding to the lithium ion migration thought the SEI film increase significantly while the charge transfer resistances increase slightly with increasing cycle number [182]. These results suggest that the layered manganese oxide film is preserved and the deformation is not obvious after cycling. According to these discoveries, the capacity fading might be attributed to the continuous growth of the SEI film which consumes the electrolyte as well as the change of SEI component to lithium fluoride with low lithium ion permeability [125]. The SEI film blocked some MnO_x from the electrochemically active component, especially at high current rate due to large polarization. $LiPF_6$ is readily decomposed in the presence of water and hydroxyls to produce HF. The presence of HF will react with Li_2CO_3 and $ROCO_2Li$ which are the general components of the SEI film to form LiF [228]. Therefore, the most important parameter to influence the cyclic stability is the trace amount of water remaining among the layers of the manganese oxide which can be confirmed form the TGA-MS results [182].

4.2.1.2. Spinel and orthosilicates. ACNTs@$LiMn_2O_4$ was fabricated as well as cathode for LIBs due to the favorable charge storage capacity, high ionic conductivity, and high discharge voltage of spinel $LiMn_2O_4$. Fig. 20(a) shows the representative charge and discharge curves at 1C (148 mA/g) over a potential range of 3.4–4.3 V vs Li^+/Li. The charge and discharge curves of ACNTs@$LiMn_2O_4$ present two distinguished plateaus, which are characteristics of spinel-type lithium manganese oxides reflected a two-stage mechanism of lithium extraction and insertion [229]. The extraction/insertion of lithium ions from/into one half of the tetrahedral sites with lithium–lithium interaction at 4.05/3.94 V vs Li^+/Li and the other half of the tetrahedral sites without lithium–lithium interaction at 4.17/4.08 V vs Li^+/Li [230]. A high initial discharge capacity of 122.1 mAh/g is achieved for this coaxial nanoarray hybrids, demonstrating the efficient utilization of the active material. The obtained materials show extremely good cyclic stability as presented in Fig. 20(b). Discharge capacities of 103.4 and 88.1 mAh/g are retained after 1000 and 2000 cycles, respectively, which corresponds 84.6% and 72.2% of the initial capacities. An initial Coulombic efficiency of 90.4% is observed which increases gradually to about 100%. There high Coulombic efficiency indicates fewer side reactions which ensures the high cyclic stability. The capacity fading of $LiMn_2O_4$ can be attributed to the dissolution of manganese due to disproportionation reaction, the formation of two cubic phases owing to structure instability, Jahn–Teller distortion resulted from severe

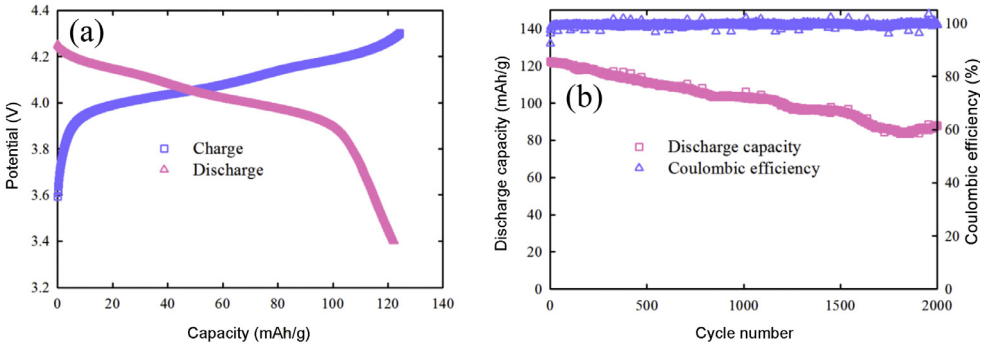

Fig. 20. (a) Charge and discharge voltage profiles and (b) cyclic stability of ACNTs@$LiMn_2O_4$ at 1 C (148 mA/g) between 3.4 and 4.3 V vs Li^+/Li.

volume change, microstrain caused by volume change etc. [230]. The core-shell nanotube structure enables the elastic deformation of the host lattice to accommodate the strain. Therefore, the mild capacity fading is probably due to the dissolution of manganese, which is consistent with the continually and slowly capacity fading phenomenon.

ACNTs@Li_2FeSiO_4/Al was prepared by coating ACNTs/Al with Li_2FeSiO_4 through a polyvinyl alcohol assisted sol-gel method. Carbon coated nanoporous Li_2FeSiO_4 (Li_2FeSiO_4/C) powder obtained under analogous conditions by a polyvinyl alcohol assisted sol-gel method was employed as a reference to demonstrate the advantages of ACNTs@Li_2FeSiO_4/Al [218]. ACNTs@Li_2FeSiO_4/Al can deliver a high specific capacity of 175 mAh/g initially, while Li_2FeSiO_4/C can only deliver a discharge capacity of 80 mAh/g at the same current rate (Fig. 21a) [218]. The high initial discharge capacity of ACNTs@Li_2FeSiO_4/Al was attributed to a combination of high specific surface area of ACNTs resulted thin Li_2FeSiO_4 film and high electrical conductivity of ACNTs resulted efficient charge transfer. Shortening in lithium ion diffusion distance in ACNTs@Li_2FeSiO_4/Al increases the utilization of active materials and thus the discharge capacity.

ACNTs@Li_2FeSiO_4/Al shows excellent rate capability as well which can deliver a high discharge capacity of 91 mAh/g at 20 C (Fig. 21b) [218]. Both SEI resistance and charge transfer resistance of ACNTs@Li_2FeSiO_4/Al are much lower than those of Li_2FeSiO_4/C (Fig. 21e and f) [218]. The Li_2FeSiO_4/C shows a straight sloping line with a 45° angle at low frequencies, corresponding to a semi-infinite Warburg diffusion process in the bulk materials. However, ACNTs@Li_2FeSiO_4/Al shows a sloping line with an angle much larger than 45° in the same frequency region, corresponding to a transition region and finite diffusion region. This indicates that lithium ion diffusion was sufficiently fast due to the short diffusion distance. According to CV curves at 12th cycle, the redox potential separation of ACNTs@Li_2FeSiO_4/Al was 0.31 V compared with 0.47 V for Li_2FeSiO_4/C, indicating the low resistance resulted low overpotential which is consistent with the discussion in Section 2 [218]. Therefore, the results of EIS and CV confirmed that the kinetics of lithium ion and electron transfer into the electrodes were much faster for ACNTs@Li_2FeSiO_4/Al, the lithium ion diffusion distance was shorter, and the polarization was weaker compared with Li_2FeSiO_4/C, indicating a stronger charge transfer reaction in ACNTs@Li_2FeSiO_4/Al which resulting in an improved rate capability [218].

The discharge capacity of ACNTs@Li_2FeSiO_4/Al decreases slightly from 144 mAh/g for the first 5 cycles, but stabilizes after the first 5 cycles and maintains a value of 142 mAh/g for the following 45 cycles, with a capacity retention of around 99% [218]. However, Li_2FeSiO_4/C shows an initial discharge capacity of 55 mAh/g only, and suffers from about 8% capacity fading after 50 cycles. Moreover, after cycling both samples for 50 times, the C rate was increased from 1 to 5, and 20 C, and run 20 cycles at each C rate, followed by a return to C/20 (Fig. 21d). ACNTs@Li_2FeSiO_4/Al presents good cyclic stability at each rate. After a total of 112 cycles, the reversible capacity at C/20 is 155 mAh/g, which shows a capacity fading of 12% compared to the initial reversible capacity of 175 mAh/g at C/20. Upon further cycling at increased C rates, the reversible capacities are still maintained at 123, 112, and 94 mAh/g at rates of 1, 5, and 20 C, respectively. Li_2FeSiO_4/C samples on the other hand, gave much lower reversible capacities (Fig. 21d). Values of 40, 25, and 8 mAh/g were measured at cycling rates of 1, 5, and 20 C, respectively. Therefore, the advantages of ACNTs based sample, in terms of high discharge capacity, good rate capability and high cyclic stability, are fully demonstrated by comparing with a conventional powder sample.

4.2.2. Anode

4.2.2.1. Aligned carbon nanotubes. ACNTs synthesized by different methods have been investigated as anodes for LIBs [146,159,176,231]. In 1998, Martin et al. firstly reported the lithium intercalation behave of ACNTs prepared by a template assisted method, which could achieve a specific capacity of 490 mAh/g [159]. A reversible capacity of 200 mAh/g was achieved for ACNTs by Zhang et al., which is lower compared with the commercial graphite because the inner graphitic layer cannot be penetrated by lithium ions [146]. However, ACNTs can deliver capacities of 75 and 24 mAh/g at 36 and 600 C, respectively, indicating their 3D structure resulted good rate capability. Besides, ACNTs have been grown on graphene paper through chemical vapor deposition as free standing electrodes for LIBs by Yang et al. [176]. A moderate discharge capacity of 290 mAh/g was achieved after 40 cycles. Capacities of 265 and 55 mAh/g were achieved at 60 and 3600 mA/g, respectively. Recently, Dai et al. achieved high discharge capacities of 782 and 166 mAh/g at current densities of 57 and 26,000 mA/g, respectively, for ACNTs [231]. A reversible capacity of 228 mAh/g has been achieved for ACNTs over stainless steel in our group, but the capacity increases slightly with cycling (Fig. 22) [184]. All the published data demonstrate that ACNTs can achieve good rate capability resulted from its highly conductive 3D nanostructures. However, the reported capacities range from 200 to 782 mAh/g. Lithium ions can be stored in ACNTs through intercalation into intratubal sites, intertubal sites, and layered graphite structures [232]. Therefore, the crystallinity, tip properties, surface properties, heteroatoms, site density, diameter etc. could be optimized to achieve high lithium ion storage performance.

4.2.2.2. Metal oxides. Metal oxides can be utilized as anode for LIBs via conversion reaction mechanism with high capacity [202]. However, the lithium ion storage performance of metal oxides is size sensitive because the extraction of lithium from lithium oxide has been shown to be only possible with the use of nano-sized materials [186]. Therefore, the preparation of fine and stable metal oxide particles become critical to ensure the high lithium ion storage capacity and good cyclic stability. The deposition of metal oxides nanoparticles over high surface area conductive substrates is a promising approach. In another one of our work, manganese oxide (MnO_x) is coated over

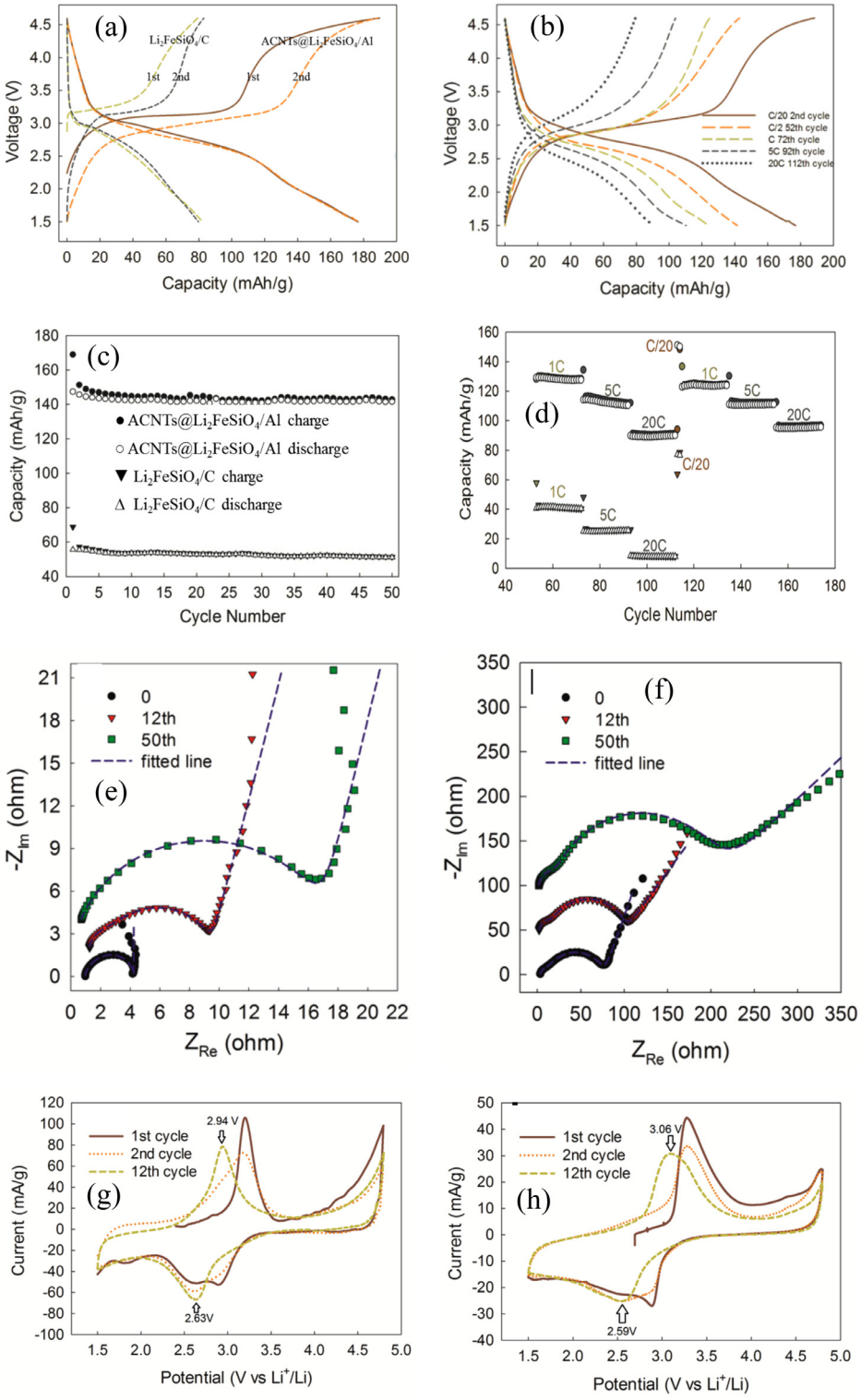

Fig. 21. (a) First 2 cycle charge and discharge voltage profiles at a current density of C/20 (C =160 mA/g) for the ACNTs@Li_2FeSiO_4/Al and Li_2FeSiO_4/C [218]. (b) The rate capability of the ACNTs@Li_2FeSiO_4/Al at current rates of 0.05, 0.5, 1, 5, and 20 C, corresponding to 2nd, 52nd, 72nd, 92nd, and 112th cycles, respectively [218]. (c) Cyclic stability of ACNTs@Li_2FeSiO_4/Al and Li_2FeSiO_4/C at 0.5C [218]. (d) Rate capability retention of the ACNTs@Li_2FeSiO_4/Al and Li_2FeSiO_4/C (the legend symbols are same as in Fig 21c) [218]. Nyquist plots of the (e) ACNTs@Li_2FeSiO_4/Al and (f) Li_2FeSiO_4/C measured before charging and at fully discharged states at 12th and 50th cycles [218]. CV profiles of the (g) ACNTs@Li_2FeSiO_4/Al and (h) Li_2FeSiO_4/C for 1st, 2nd, and 12th cycles at 0.1 mV/s and between 1.5 and 4.8 V vs Li^+/Li.

ACNTs/stainless steel foil as anodes for LIBs and the effect of carbon coating on the performance was investigated [184].

Obviously, the carbon coated sample (ACNTs@MnO_y@C) has better cyclic stability compared with the one without carbon coating (ACNTs@MnO_x) (Fig. 23a and b). The 100 cycles' average Coulombic efficiency of the ACNTs@MnO_y@C (98.1%) is higher than that of the ACNTs@MnO_x (97.5%), indicating less side reactions taken place after carbon coating. The presence of the carbon layer improves the Coulombic efficiency by blocking liquid electrolyte penetration to the MnO_y surface which can partially suppress the formation of SEI film

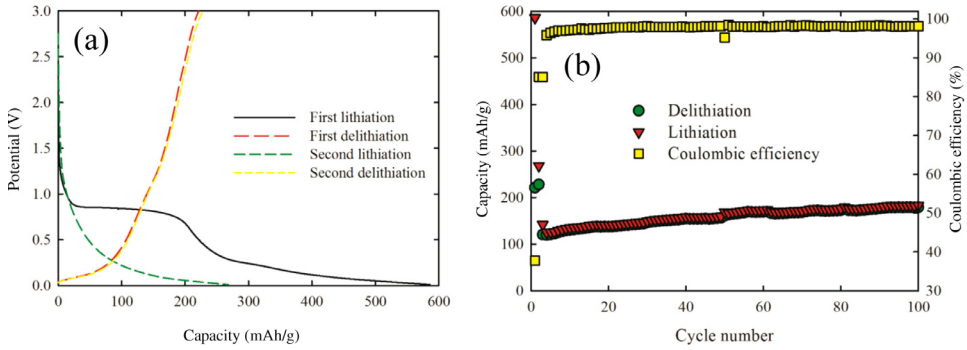

Fig. 22. (a) The first 2 cycles' voltage profiles of ACNTs at a current density of 60 mA/g between 0.01 and 3.0 V vs Li^+/Li. (b) Cyclic stability of ACNTs at a current density of 60 mA/g for the first two cycles and 600 mA/g for the following cycles between 0.01 and 3.0 V vs Li^+/Li [184].

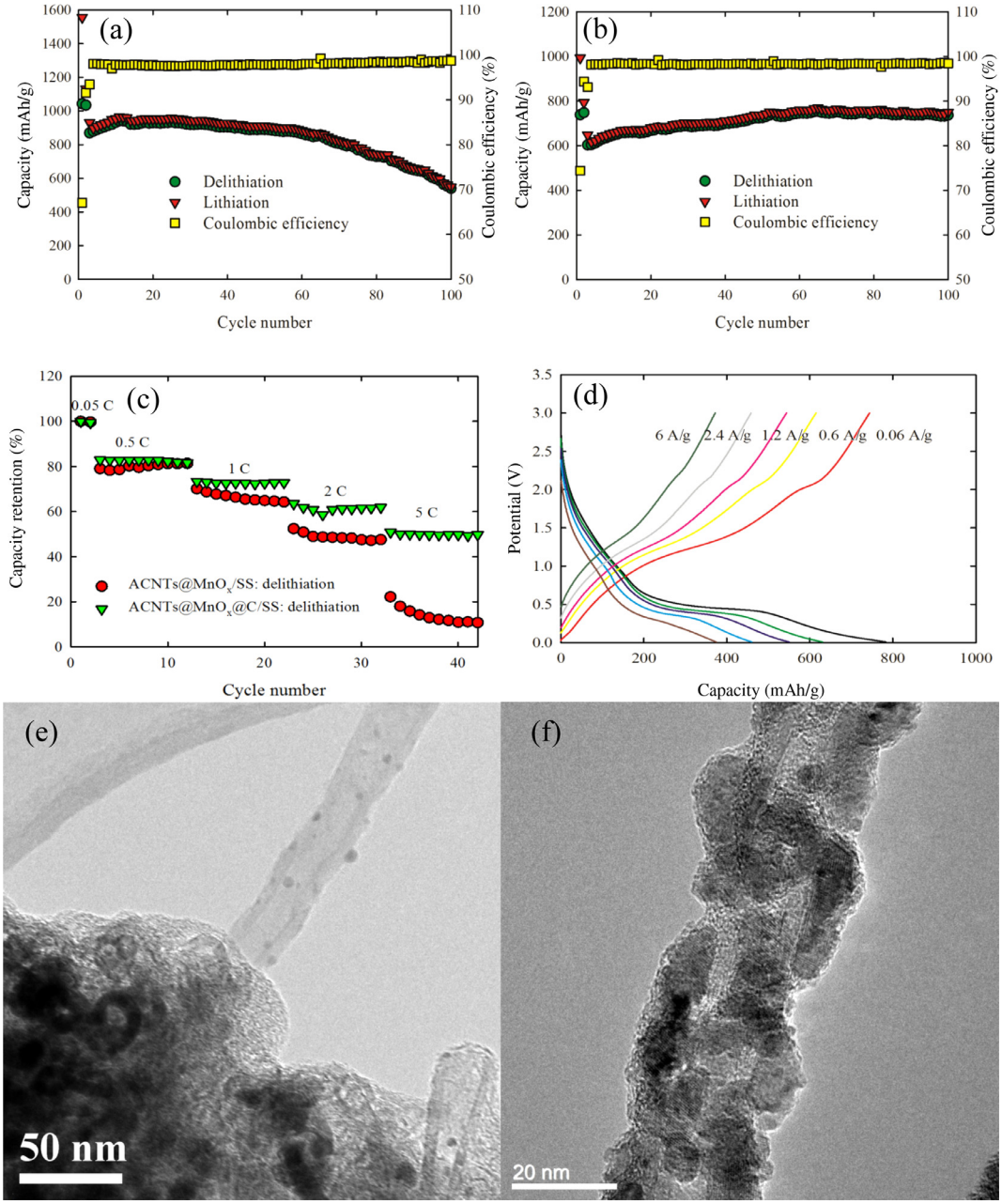

Fig. 23. Cyclic stability of the (a) ACNTs@MnO_x and (b) ACNTs@MnO_y@C at a current density of 60 mA/g for the first two cycles and 600 mA/g for the following cycles between 0.01 and 3.0 V vs Li^+/Li. (c) Rate capability of materials obtained. (d) Charge and discharge voltage profiles of ACNTs@MnO_y@C at various current densities. TEM images of (e) the ACNTs@MnO_x and (f) the ACNTs@MnO_y@C after 100 cycles at 600 mA/g between 0.01 and 3 V vs Li^+/Li [184].

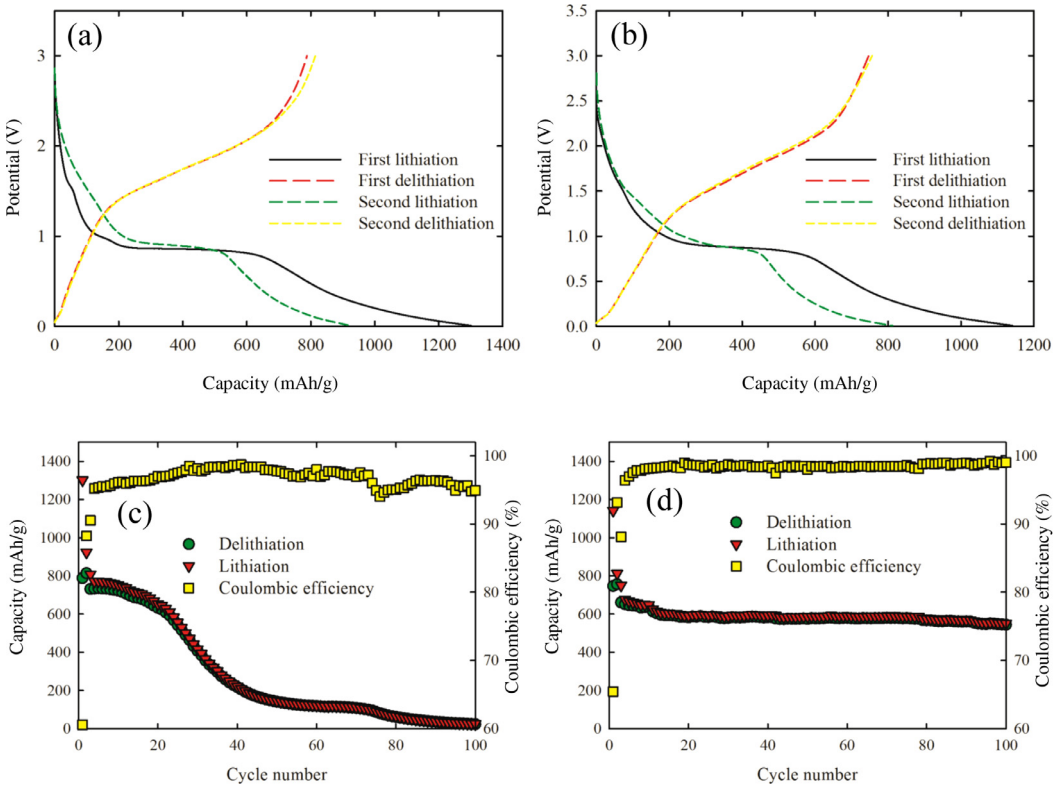

Fig. 24. The first 2 cycles' voltage profiles of (a) ACNTs@FeO_x and (b) ACNTs@FeO_x@C cycled at a current density of 50 mA/g between 0.01 and 3.0 V vs Li^+/Li. Cyclic stability of the (c) ACNTs@FeO_x and (d) ACNTs@FeO_x@C at a current density of 50 mA/g for the first two cycles and 500 mA/g for the following cycles between 0.01 and 3.0 V vs Li^+/Li [184].

[233]. The ACNTs@MnO_y@C can deliver a high specific capacity of 737 mAh/g at 600 mA/g, even after 100 cycles, which is as high as the initial specific capacity. This value is one time higher than the theoretical capacity of graphite which is used as anodes for commercial LIBs.

The cycled cells were disassembled to investigate the mechanism behind stability improvement after carbon coating. A significant aggregation occurred for the ACNTs@MnO_x during cycling (Fig. 23e). Solid reactions at the interface between two nanoparticles are typically involved in the aggregation. The volume of MnO_x film is expected to be expanded significantly during lithiation due to its high lithium storage capacity. It seems that the volume of the film was enlarged so significant that an interface formed between the adjunct MnO_x films. A slow solid reaction caused aggregation. After 100 cycles, large particles were formed from several pieces of original MnO_x thin films as shown in Fig. 23(e). Coating one layer of stable material such as carbon is a powerful strategy to suppress the formation of the interface between MnO_x and thus the aggregation. In this regards, it is crucial to form a uniform carbon layer to cover whole surface of MnO_x film. Chemical vapor deposition carbon coating process is obviously a preferred method to achieve this objective.

In addition to the high specific capacity and good cyclic stability, manganese oxide exhibits a good rate capability as well after carbon coating, as presented in Fig. 23(e) and (f). ACNTs@MnO_y@C shows better rate performance compared with ACNTs@MnO_x especially at high current densities. It is worth noting that the capacity retention of ACNTs@MnO_y@C is about 50% at a high current density of 6000 mA/g corresponding to a capacity of 374 mAh/g. This value is even higher than the theoretical capacity of graphite. However, the capacity retention of ACNTs@MnO_x is only about 10% at the same current density. The rate capability of ACNTs@MnO_y@C is much better than the reported value for MnO_x/CNTs [207].

The excellent rate capability of obtained MnO_x can be ascribed to its unique structure. The ACNTs increase the electrical conductivity of obtained electrodes and forms regular mesoporous channel which decreases the charge diffusion resistance. The MnO_x thin film decreases the electron and lithium ion diffusion distance significantly. The outer carbon layer increases the electrical conductivity of obtained electrode further and prevents the aggregation which maintains the mesoporous channel between carbon nanotubes.

Iron oxide was coated over ACNTs via spontaneous reduction of K_2FeO_4 followed by annealing in argon and acetylene to obtain ACNTs@FeO_x and ACNTs@FeO_x@C, respectively. The lithium ion storage capacities of ACNTs@FeO_x and ACNTs@FeO_x@C were evaluated by charging and discharging at a current density of 50 mA/g between 0.01 and 3 V vs Li^+/Li (Fig. 24a and b). The initial lithiation and delithiation capacities of ACNTs@FeO_x are found to be 1301 and 788 mAh/g, respectively, with a Coulombic efficiency of 60.5%. The initial lithiation and delithiation capacities decrease to 1141 and 746 mAh/g, respectively, after carbon coating, while the Coulombic efficiency increases to 65.4%. Hence, the initial Coulombic efficiency increases slightly after carbon coating.

The cyclic stability of ACNTs@FeO_x and ACNTs@FeO_x@C was tested at a current density of 50 mA/g for the first two cycles and 500 mA/g for the following cycles between 0.01 and 3.0 V vs Li^+/Li (Fig. 24c and d). ACNTs@FeO_x surfers from serious capacity fading after only 20 cycles and a capacity of 23 mAh/g is left after 100 cycles. The cyclic stability improves significantly after carbon coating. After a mild capacity fading at the beginning, the capacity stabilizes at about 550 mAh/g. ACNTs@FeO_x@C shows excellent rate capability as well and it can deliver a capacity of 470 mAh/g at a high current density of 2 A/g. Therefore, the electrochemical performance of iron oxide improves significantly after carbon coating. The results clearly confirm our strategy of the rational electrode design.

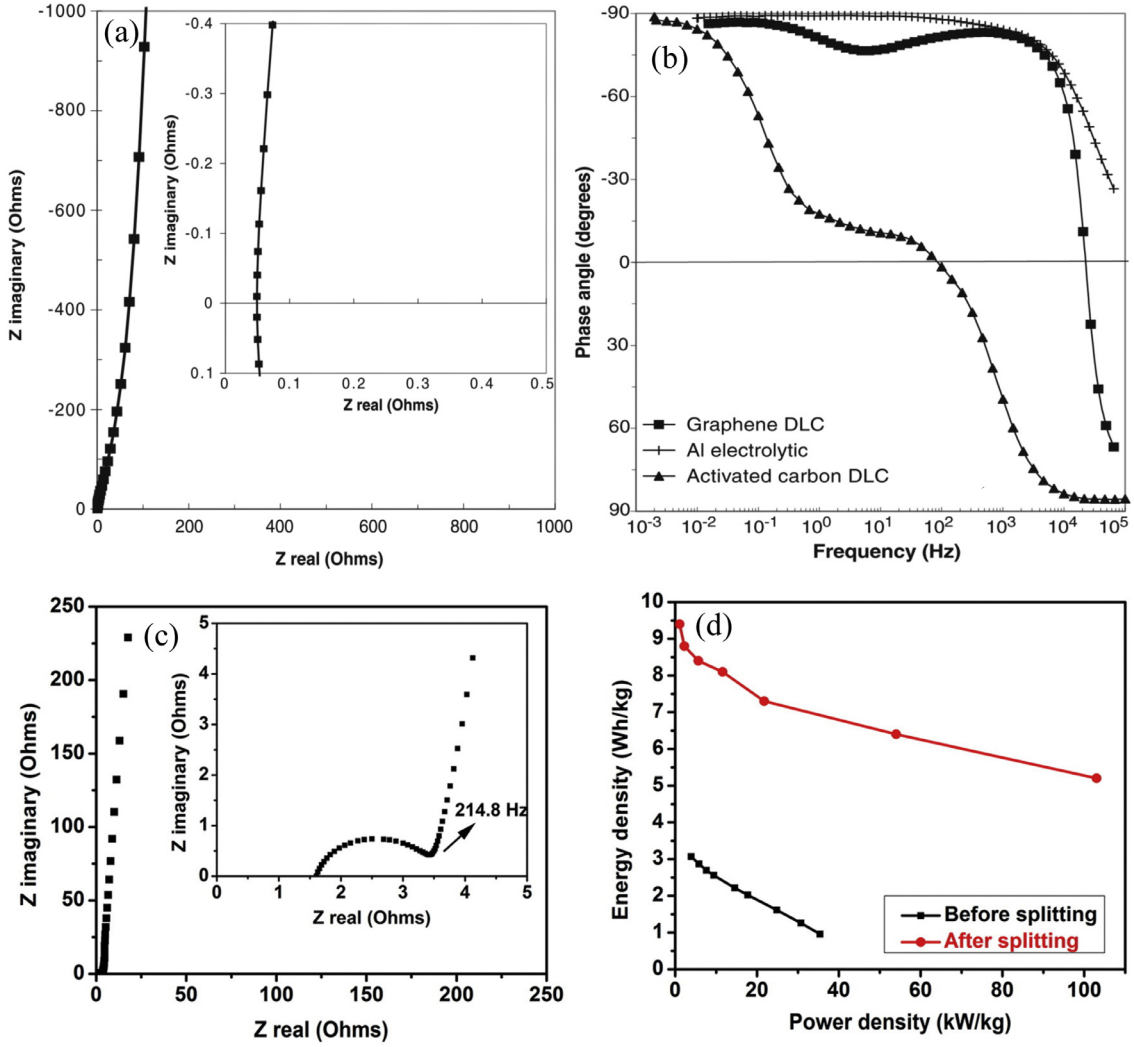

Fig. 25. (a) Nyquist plot of the aligned graphene arrays based capacitor. (b) Comparison of impedance phase angle data of aligned graphene based capacitor, commercial activated carbon based capacitor, and an aluminum electrolytic capacitor [238]. (c) Nyquist plot of the aligned graphene nanoribbon based capacitor. (d) Ragone plot showing the relationship between the energy density and power density of the aligned graphene nanoribbon capacitor [242].

Accordingly, ACNTs based 3D electrodes exhibit excellent electrochemical performance for both SCs and LIBs. This can be ascribed to the high electrical conductivity of ACNTs and their good contact with current collectors which decrease the internal resistance significantly, the regular channels formed among ACNTs resulted enhanced mass transfer in the electrolyte, and the thin electrochemically active film which decreases the ion diffusion distance. Therefore, ACNTs based 3D electrodes shows promising applications for electrochemical energy storage.

5. Extended to aligned graphene arrays

Graphene, a two dimensional monolayer of sp^2-hybrided carbon sheet, attracts huge amount of interest for energy storages due to its high electrical conductivity, large specific surface area, and high chemical stability [234]. Aligned graphene arrays, which are initially called carbon nanowalls, are a type of 3D structures which compose of graphene vertically standing on a substrate [235,236]. They attract increasing attention for energy storages due to their unique structure resulted high electrochemical performance [237–242]. The principles for electrode rational design obtained from ACNTs can be extended further to aligned graphene arrays.

The synthesis of aligned graphene nanosheets directly on heated nickel substrates by utilizing radio frequency plasma-enhanced chemical vapor deposition for SCs was first reported by Miller and co-workers [238]. According to the Nyquist plot of aligned graphene as shown in Fig. 25(a), there is neither evidence of porous electrode behavior nor features associated with series-passive layer. Data fit a near vertical line as produced by a series-*RC* circuit with the intersect with the real axial as low as about 0.05 Ω [238]. The comparison of impedance phase angle data of aligned graphene based capacitor, commercial activated carbon based capacitor, and an aluminum electrolytic capacitor is presented in Fig. 25(b). The impedance phase angles of the graphene capacitor, activated carbon capacitor, and aluminum electrolytic capacitor are -82°, ~0°, and -83°, respectively, at 120 Hz, indicating the fast frequency response of the aligned graphene based capacitor and thus high rate capability [238]. Recently, Tour and co-workers reported the split of ACNTs to generate aligned graphene nanoribbons by utilizing potassium vapor for SCs [242]. The Nyquist plot exhibits a semicircle intersecting the real axis in the high frequency region, suggesting a distributed capacitance behavior of a porous structure at high frequency, and an almost vertical line in the low frequency region, implying a capacitive behavior at low frequencies (Fig. 25c) [242]. The knee frequency is as high as 214.8 Hz, indicating most of the stored energy is accessible

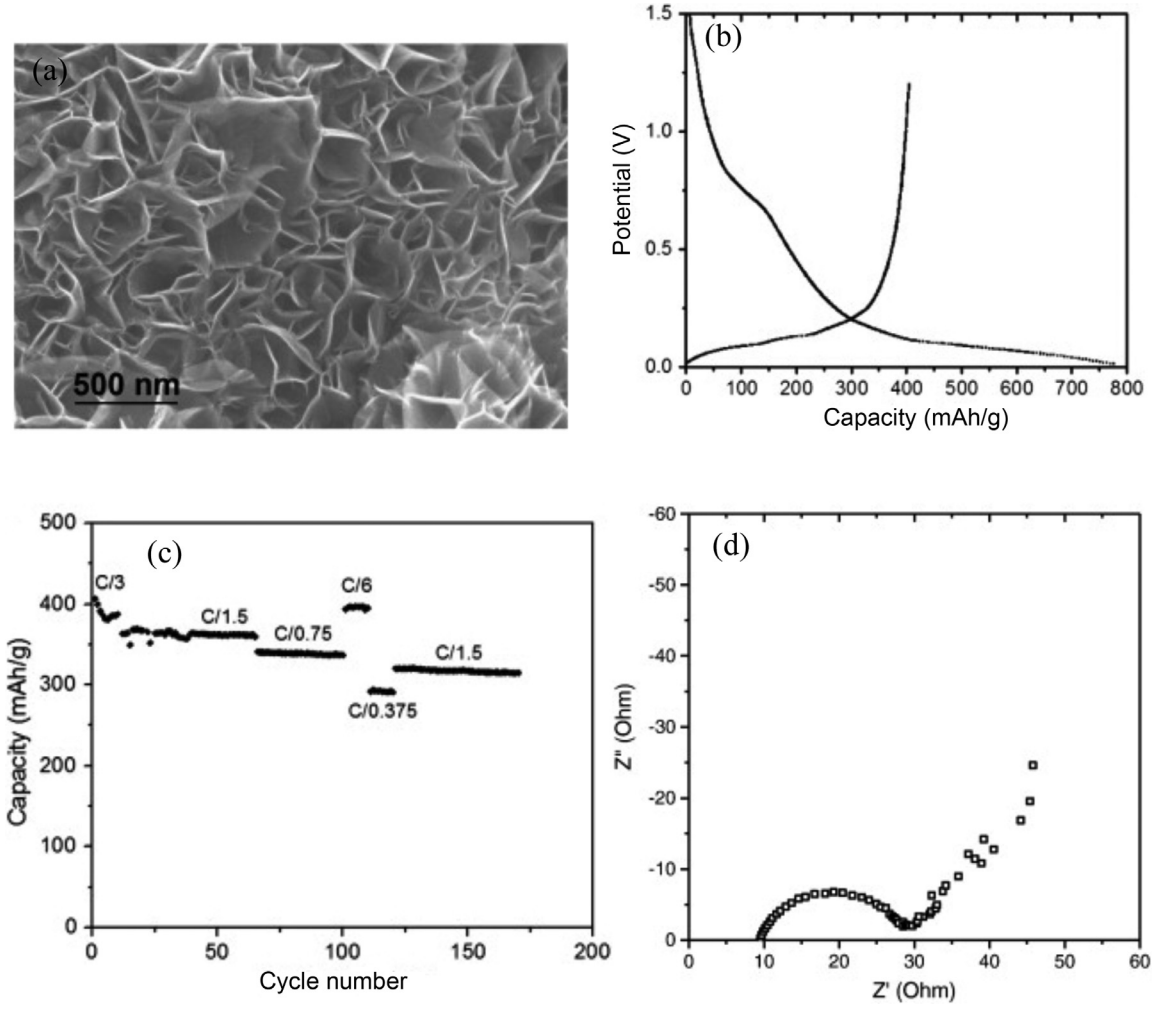

Fig. 26. (a) SEM image, (b) first cycle discharge and charge voltage profiles, (c) capacity retention, and (d) Nyquist plot of the aligned graphene arrays as anode electrode for LIBs [239].

even at frequencies ≥ 210 Hz, which might be the result of fast electrolyte ions access and diffusion through the regular channels formed between aligned graphene nanoribbons [242]. As shown in the Ragone plot (Fig. 25d), the aligned graphene nanoribbons based SCs exhibit the specific energy and specific power in the range of 5.2–9.4 Wh/kg and 1.1–103 kW/kg, respectively, which are much higher than those of ACNTs. The primary reason for this phenomenon is the fact that graphene has much higher specific surface area than carbon nanotubes.

Additionally, aligned graphene arrays have also been explored as anode materials for LIBs. Rao and co-workers reported the synthesis of aligned graphene arrays over metal substrates by utilizing plasma-enhanced chemical vapor deposition as anodes for LIBs [241]. The graphene nanosheet possesses a flower like morphology and exhibits a reversible capacity of 637 mAh/g after 50 cycles [241]. The electrodes also give better cyclic stability and rate capability [241]. Chen et al. claimed the synthesis of highly branched graphene nanosheet arrays directly on copper current collector as anode materials for LIBs [240]. The graphene nanosheet arrays show high capacities of 461 mAh/g after 100 cycles and 297 mAh/g at 4 C, which indicates good cyclic stability and rate capability [240]. Besides, Xiao et al. also demonstrated the synthesis of aligned graphene arrays on nickel foil utilizing microwave plasma-enhanced chemical vapor deposition as anodes for LIBs [239]. The aligned graphene sheet is in the range of several microns with channels formed between them (Fig. 26a) [239]. A reversible capacity of 380 mAh/g was observed initially (Fig. 26b) with limited capacity loss over 150 cycles (Fig. 26c) [239]. Additionally, a reversible capacity of 280 mAh/g was achieved at a high rate of C/0.375, demonstrating the good rate capability of the aligned graphene electrode due to the reduced diffusion distance [239]. The Nyquist plot demonstrated the enhanced electrical conductivity due to the effective connection to the current collector (Fig. 26d) [239]. However, the irreversible capacity loss in the first cycle is more than 50% for the mentioned aligned graphene as anodes for LIBs. This is generally observed for graphene based anode for LIBs which might be attributed to electrolyte decomposition and formation of SEI film due to the large surface area and the irreversible reaction of lithium ions with residual oxygen functional groups [239–241].

Recently, Wang and co-workers reported the synthesis of aligned graphene@GeO_x sandwiched arrays over copper foil as anodes for LIBs [237]. Aligned graphene was synthesized by plasma-enhanced chemical vapor deposition process. Micron level interspaces (Fig. 27a) were generated between graphene sheets which have the thickness in the range of 3–4 layers (Fig. 27b). Subsequently, GeO_x was coated over aligned graphene by a thermal Ge/Sn co-evaporation method. The sandwiched structure of graphene coated with GeO_x can be clearly observed from Fig. 27(c). The aligned graphene@GeO_x sandwiched structure arrays show high cyclic stability as anodes for LIBs no matter the GeO_x loading is 70 wt% or 61 wt% (Fig. 27d). However, the sample with 79 wt% GeO_x loading cannot achieve the

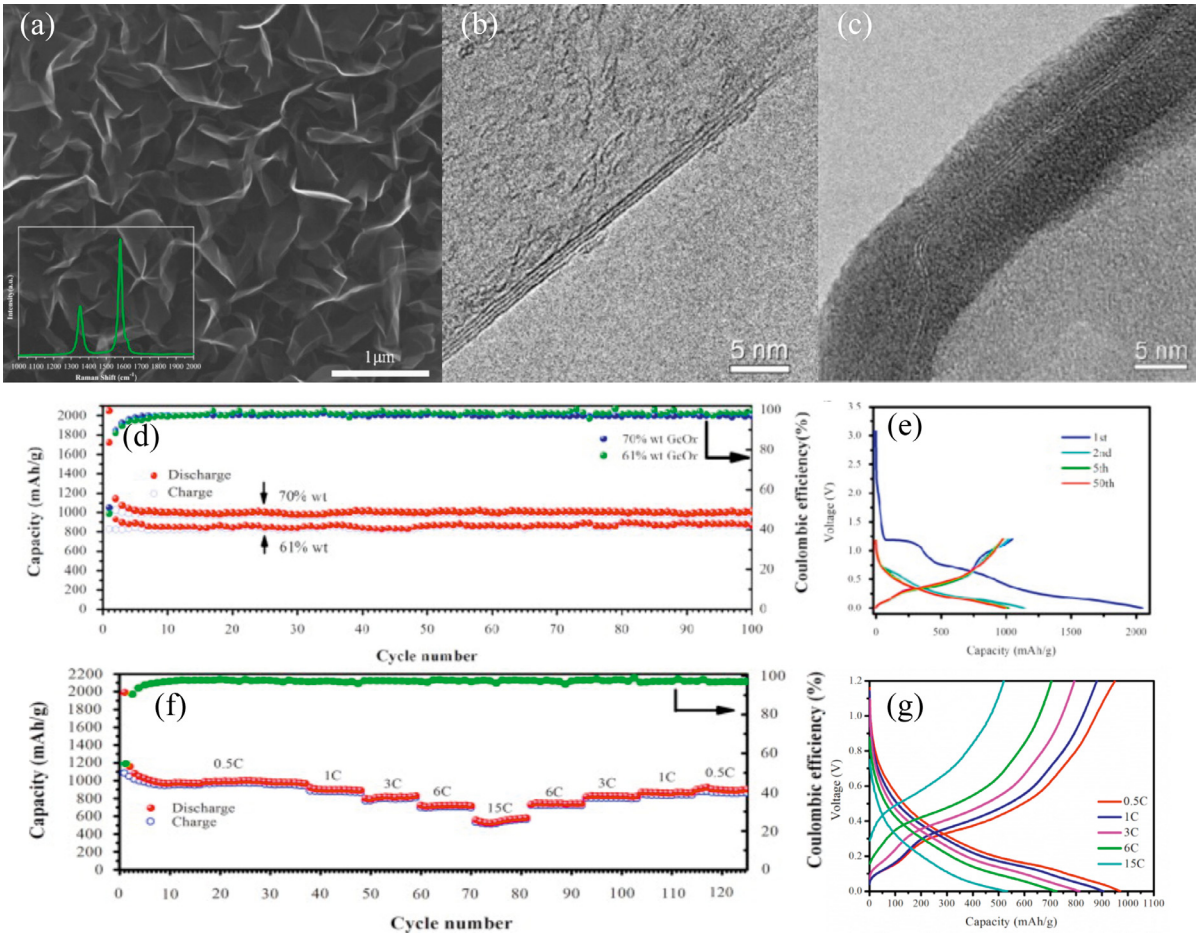

Fig. 27. (a) SEM and (b) TEM images of the aligned graphene. (c) TEM image of aligned graphene@GeO_x. (d) Cyclic stability of aligned graphene@GeO_x with different GeO_x loadings, 70 wt% and 61 wt%, both tested at the rate of C/3. (e) Voltage profiles of the electrode assembled with a 70 wt% GeO_x load. (f) Rate performance of the electrode (70 wt% GeO_x) at the rates of 0.5 C, 1 C, 3 C, 6 C, 15 C, respectively. (g) Voltage profiles of the electrode corresponding to the rate performance test [237].

theoretical capacity which might be because part of GeO_x detaches from aligned graphene [237]. The sample with 70 wt% GeO_x can deliver a high capacity of 1008 mAh/g after 100 cycles with capacity retention of 96%. However, the capacity is even higher than the theoretical value. The authors ascribed this to the interfacial lithium ion storage contribution due to the large interfaces between graphene and GeO_x [237]. According to the initial voltage profiles (Fig. 27e), the discharge and charge capacities are 2049 and 1047 mAh/g resulting in a very low initial Coulombic efficiency of 51.1%. The aligned graphene@GeO_x sandwiched arrays show an improved rate capability which can deliver a high specific capacity of 545 mAh/g even at 15C (Fig. 27f and g), indicating the sandwiched arrays resulted improved electron and lithium ion transport [237].

Therefore, aligned graphene and its composites exhibit again excellent electrochemical performances as electrodes for electrochemical energy storages. This can be similarly ascribed to the highly electrical conductivity of graphene and its direct contact with current collet resulted low internal resistance, regular channel formed between graphene sheets caused low mass transfer resistance, and thin active film resulted short ion diffusion distance. Accordingly, the principles for electrode rational design obtained from ACNTs can be safely extended to aligned graphene arrays.

Aligned graphene arrays are characterized by the following features as electrodes for energy storage relative to ACNTs. Firstly, the mass loading of aligned graphene arrays grown over conductive substrates is normally lower relative to ACNTs due to the fact that they are much shorter. This results in a lower specific energy if it is calculated based on the total mass of the electrode. Additionally, the alignment of aligned graphene array is generally poorer compared with ACNTs. With the development of chemical vapor deposition techniques, super-ACNTs can be synthesized by carefully controlling the experimental conditions. However, this is very difficult to be realized for aligned graphene arrays. The poor alignment of aligned graphene arrays increases pore tortuosity and thus decreasing mass transfer and specific power. Aligned graphene arrays can be prepared by a cheap solution based method by exfoliation of graphite followed by assembling on conductive substrates [243]. However, ACNTs are normally synthesized by chemical vapor deposition which is relatively expensive. Furthermore, the specific surface area of aligned graphene is normally higher than that of ACNTs. This is the reason why aligned graphene based composites can reach theoretical specific capacity/capacitance with relatively high loading.

6. Summary and outlook

This paper provides a comprehensive overview of the most recent developments on the synthesis and applications of aligned carbon nanostructures based electrodes for SCs and LIBs. The active materials coated aligned carbon nanostructures show very promising applications in electrochemical energy storage resulted from the unique 3D structures. The electrochemically active material is used to store energy, while the aligned carbon nanostructures is employed to provide a large surface area to support the active material and the nanocable array to facilitate the electron transport as well as forming regular channels to facilitate mass transfer in the electrolytes. The thin film of active materials can not only reduce ion transfer resistance by

shortening the diffusion distance but also make the film elastic enough to tolerate significant volume change during charge and discharge cycles. The conductive substrate is used directly as the current collector and the direct contact of the aligned carbon nanoarrays with the substrate significantly reduces the contact resistance.

Although many proof-of-concept studies have demonstrated the superior performance of aligned carbon nanostructure based electrodes for electrochemical energy storage, challenges still exist which prevent the wide applications. The main challenges arise from the materials themselves which limited the methods for active materials coating. High temperature annealing process is not allowed in the presence of oxidizing agent, such as oxygen and metal oxide, because ACNTs can be oxides or the active materials could be reduced. Therefore, we have not found any reports with regard to the synthesis of ACNTs coated $LiFePO_4$ or $LiCoO_2$, which are widely used for LIBs. In addition, the presence of metal foil also limits the methods for active material coating. Metal foil can be oxided or dissolved in some specific solutions, for instance Al can be dissolved in basic solution or in the presence of halogens. Moreover, the growth of superlong ACNTs directly over metal foil is still a challenge which results in the low active material loading relative to the current collectors. Additionally, it is still hard to grow well ACNTs over copper and graphite foils which has been widely utilized as current collectors for electrochemical energy storage.

Generally, ACNTs and graphene arrays over conductive substrates are synthesized through chemical vapor deposition, which are usually operated at elevated temperatures. It not only increases the production cost but also limits the selection of conductive substrate. Solution based method will be a green and efficient approach for the large scale production of high quality aligned carbon nanostructures, as confirmed by a very recent work by Yang and co-workers [243]. Hence, solution based method will be a new trend for the growth of high quality aligned carbon nanostructures for EES.

Acknowledgments

The facility support from NTNU Nanolab and financial supports from VISTA, Zhengzhou Research Institute of Chalco and Norwegian research council are gratefully acknowledged.

References

[1] B. Dunn, H. Kamath, J.-M. Tarascon, Science 334 (6058) (2011) 928.
[2] J.M. Tarascon, M. Armand, Nature 414 (6861) (2001) 359.
[3] S. Chu, A. Majumdar, Nature 488 (7411) (2012) 294.
[4] M. Armand, J.M. Tarascon, Nature 451 (7179) (2008) 652.
[5] H. Jiang, P.S. Lee, C. Li, Energy Environ. Sci. 6 (1) (2013) 41.
[6] R. Liu, J. Duay, S.B. Lee, Chem. Commun. 47 (5) (2011) 1384.
[7] J.B. Goodenough, Y. Kim, Chem. Mater. 22 (3) (2009) 587.
[8] B.E. Conway, Electrochemical Supercapacitors: Scientific Fundamentals and Technological Applications, Kluwer Academic, New York, 1999, p. 698.
[9] B.J. Andrew, Power Sources 91 (1) (2000) 37.
[10] W. Wei, X. Cui, W. Chen, D.G. Ivey, Chem. Soc. Rev. 40 (3) (2011) 1697.
[11] G. Wang, L. Zhang, J. Zhang, Chem. Soc. Rev. 41 (2) (2011) 797.
[12] B. Scrosati, J. Hassoun, Y.-K. Sun, Energy Environ. Sci. 4 (9) (2011) 3287.
[13] O.K. Park, Y. Cho, S. Lee, H.-C. Yoo, H.-K. Song, J. Cho, Energy Environ. Sci. 4 (5) (2011) 1621.
[14] L. Ji, Z. Lin, M. Alcoutlabi, X. Zhang, Energy Environ. Sci. 4 (8) (2011) 2682.
[15] G. Jeong, Y.-U. Kim, H. Kim, Y.-J. Kim, H.-J. Sohn, Energy Environ. Sci. 4 (6) (2011) 1986.
[16] X.-P. Gao, H.-X. Yang, Energy Environ. Sci. 3 (2) (2010) 174.
[17] V. Etacheri, R. Marom, R. Elazari, G. Salitra, D. Aurbach, Energy Environ. Sci. 4 (9) (2011) 3243.
[18] P. Novák, K. Müller, K.S.V. Santhanam, O. Haas, Chem. Rev. 97 (1) (1997) 207.
[19] P. Simon, Y. Gogotsi, Nat. Mater. 7 (11) (2008) 845.
[20] J.R. Miller, P. Simon, Science 321 (5889) (2008) 651.
[21] B.Z. Jang, C. Liu, D. Neff, Z. Yu, M.C. Wang, W. Xiong, A. Zhamu, Nano Lett 11 (9) (2011) 3785.
[22] X. Li, B. Wei, Nano Energy 2 (2) (2013) 159.
[23] Y. Zhu, S. Murali, M.D. Stoller, K.J. Ganesh, W. Cai, P.J. Ferreira, A. Pirkle, R.M. Wallace, K.A. Cychosz, M. Thommes, D. Su, E.A. Stach, R.S. Ruoff, Science 332 (6037) (2011) 1537.
[24] E.S. Snow, F.K. Perkins, E.J. Houser, S.C. Badescu, T.L. Reinecke, Science 307 (5717) (2005) 1942.
[25] M.-J. Deng, J.-K. Chang, C.-C. Wang, K.-W. Chen, C.-M. Lin, M.-T. Tang, J.-M. Chen, K.-T. Lu, Energy Environ. Sci. 4 (10) (2011) 3942.
[26] F.B. Sillars, S.I. Fletcher, M. Mirzaeian, P.J. Hall, Energy Environ. Sci. 4 (3) (2011) 695.
[27] Y. Chen, X. Zhang, H. Zhang, X. Sun, D. Zhang, Y. Ma, RSC Adv. 2 (20) (2012) 7747.
[28] S. Chen, J. Zhu, X. Wu, Q. Han, X. Wang, ACS Nano 4 (5) (2010) 2822.
[29] A. Ghosh, E.J. Ra, M. Jin, H.-K. Jeong, T.H. Kim, C. Biswas, Y.H. Lee, Adv. Funct. Mater. 21 (13) (2011) 2541.
[30] Z.-S. Wu, D.-W. Wang, W. Ren, J. Zhao, G. Zhou, F. Li, H.-M. Cheng, Adv. Funct. Mater. 20 (20) (2010) 3595.
[31] J. Liu, J. Jiang, C. Cheng, H. Li, J. Zhang, H. Gong, H.J. Fan, Adv. Mater. 23 (18) (2011) 2076.
[32] F. Huang, F. Lou, D. Chen, ChemSusChem 5 (5) (2012) 888.
[33] F. Huang, D. Chen, Energy Environ. Sci. 5 (2) (2012) 5833.
[34] C. Liu, Z. Yu, D. Neff, A. Zhamu, B.Z. Jang, Nano Lett 10 (12) (2010) 4863.
[35] P. Arora, R.E. White, M. Doyle, J. Electrochem. Soc. 145 (10) (1998) 3647.
[36] B. Marinho, M. Ghislandi, E. Tkalya, C.E. Koning, G. de With, Powder Technol 221 (0) (2012) 351.
[37] F. Béguin, E. Frackowiak (Eds.), Supercapacitors: Materials, Systems, and Applications, Wiley-VCH Verlag GmbH & Co., 2013.
[38] L. Fenghua, S. Jiangfeng, Y. Huafeng, G. Shiyu, Z. Qixian, H. Dongxue, I. Ari, N. Li, Nanotechnology 20 (45) (2009) 455602.
[39] A.S. Chizhov, M.N. Rumyantseva, A.M. Gaskov, Inorg. Mater. 49 (10) (2013) 1000.
[40] D. Sarkar, G.G. Khan, A.K. Singh, K. Mandal, J. Phys. Chem. C 117 (30) (2013) 15523.
[41] B.M. Warnes, F.F. Aplan, G. Simkovich, Solid State Ionics 12 (0) (1984) 271.
[42] D. Bélanger, T. Brousse, J.W. Long, Electrochem. Soc. Interf. 17 (1) (2008) 49.
[43] M. Zhi, C. Xiang, J. Li, M. Li, N. Wu, Nanoscale 5 (1) (2012) 72.
[44] C. Zhou, Y. Zhang, Y. Li, J. Liu, Nano Lett 13 (5) (2013) 2078.
[45] G.M. Joshi, M. Pai, H.R. Harrison, C.J. Sandberg, R. Aragón, J.M. Honig, Mater. Res. Bull. 15 (11) (1980) 1575.
[46] C.-C. Hu, W.-C. Chen, K.-H. Chang, J. Electrochem. Soc. 151 (2) (2004) A281.
[47] L. Cao, F. Xu, Y.Y. Liang, H.L. Li, Adv. Mater. 16 (20) (2004) 1853.
[48] J. Ji, L.L. Zhang, H. Ji, Y. Li, X. Zhao, X. Bai, X. Fan, F. Zhang, R.S. Ruoff, ACS Nano 7 (7) (2013) 6237.
[49] J. Stejskal, R.G. Gilbert, Pure Appl. Chem. 74 (5) (2002) 857.
[50] H.C. Kang, K.E. Geckeler, Polymer 41 (18) (2000) 6931.
[51] L. Groenendaal, F. Jonas, D. Freitag, H. Pielartzik, J.R. Reynolds, Adv. Mater. 12 (7) (2000) 481.
[52] E. Frackowiak, Q. Abbas, F. Béguin, J. Energy Chem. 22 (2) (2013) 226.
[53] Y. Zhai, Y. Dou, D. Zhao, P.F. Fulvio, R.T. Mayes, S. Dai, Adv. Mater. 23 (42) (2011) 4828.
[54] Q. Cheng, J. Tang, J. Ma, H. Zhang, N. Shinya, L.-C. Qin, PCCP 13 (39) (2011) 17615.
[55] A.J. Bard, L.R. Faulkner (Eds.), Electrochemical Methods: Fundamentals and Applications, John Wiley & Sons, Inc, 2005.
[56] K.E. Aifantis, S.A. Hackney, R.V. Kumar (Eds.), High Energy Density Lithium Batteries Materials, Engineering, Applications, Wiley-VCH Verlag GmbH & Co. KGaA, Weinheim, 2010.
[57] M. Winter, R.J. Brodd, Chem. Rev. 104 (10) (2004) 4245.
[58] C.-X. Zu, H. Li, Energy Environ. Sci. 4 (8) (2011) 2614.
[59] D. Aurbach, M.D. Levi, E. Levi, H. Teller, B. Markovsky, G. Salitra, U. Heider, L. Heider, J. Electrochem. Soc. 145 (9) (1998) 3024.
[60] M. Park, X. Zhang, M. Chung, G.B. Less, A.M. Sastry, J. Power Sources 195 (24) (2010) 7904.
[61] P. He, X. Zhang, Y.-G. Wang, L. Cheng, Y.-Y. Xia, J. Electrochem. Soc. 155 (2) (2008) A144.
[62] T. Kawakami, N. Takahashi, M. Yamakaji. *United States Patent US* 2011/0229757A1, 2011.
[63] Y. Idemoto, T. Matsui, Solid State Ionics 179 (17–18) (2008) 625.
[64] J. Molenda, P. Wilk, J. Marzec, Solid State Ionics 146 (1–2) (2002) 73.
[65] G. Pistoia, S. Panero, M. Tocci, R.V. Moshtev, V. Manev, Solid State Ionics 13 (4) (1984) 311.
[66] M. Deka, A. Kumar, J. Solid State Electrochem. 14 (9) (2010) 1649.
[67] Z. Chen, S. Qiu, Y. Cao, J. Qian, X. Ai, K. Xie, X. Hong, H.X. Yang, J. Mater. Chem. A 1 (16) (2013) 4988.
[68] S. Franger, S. Bach, J. Farcy, J.P. Pereira-Ramos, N. Baffier, J. Power Sources 109 (2) (2002) 262.
[69] S. Dorfler, M. Hagen, H. Althues, J. Tubke, S. Kaskel, M.J. Hoffmann, Chem. Commun. 48 (34) (2012) 4097.
[70] X. Ji, K.T. Lee, L.F. Nazar, Nat. Mater. 8 (6) (2009) 500.
[71] L. Wang, J. Zhao, X. He, C. Wan, Electrochim. Acta 56 (14) (2011) 5252.
[72] L. Kavan, J. Procházka, T.M. Spitler, M. Kalbáč, M. Zukalová, T. Drezen, M. Grätzel, J. Electrochem. Soc. 150 (7) (2003) A1000.
[73] J. Wolfenstine, D. Foster, J. Read, S. Zhang, J.L. Allen, Effects of Doping and/or Atmosphere on the Electrical Conductivity of $Li_4Ti_5O_{12}$, U.S. Army Research Laboratory, 2008.
[74] J. Li, M. Zou, Y. Zhao, Y. Lin, H. Lai, L. Guan, Z. Huang, Electrochim. Acta 111 (0) (2013) 165.
[75] Z. Cao, B. Wei, J. Power Sources 241 (0) (2013) 330.
[76] D. Varshney, A. Yogi, J. Mol. Struct. 995 (1–3) (2011) 157.
[77] A. Arenst Andreas, L. Joong Kee, Phys. Scr. 2010 (T139) (2010) 014013.
[78] T.Y. Kim, H.W. Lee, M. Stoller, D.R. Dreyer, C.W. Bielawski, R.S. Ruoff, K.S. Suh, ACS Nano 5 (1) (2010) 436.
[79] H. Zhou, D. Li, M. Hibino, I. Honma, Angew. Chem. Int. Ed. 44 (5) (2005) 797.

[80] Y. Wang, H. Li, P. He, E. Hosono, H. Zhou, Nanoscale 2 (8) (2010) 1294.
[81] A.J. Bard, L.R. Faulkner, Electrochemical Methods: Fundamentals and Applications, John Wiley & Sons, Inc., 2001.
[82] R. de Levie, Electrochim. Acta 8 (10) (1963) 751.
[83] R. Kötz, M. Carlen, Electrochim. Acta 45 (15–16) (2000) 2483.
[84] F. Béguin, E. Frackowiak (Eds.), Carbons for Electrochemical Energy Storage and Conversion Systems, CRC Press, Taylor and Francis Group, LLC, Boca Raton, 2010.
[85] D. Qu, J. Power Sources 109 (2) (2002) 403.
[86] M.V. Reddy, T. Yu, C.H. Sow, Z.X. Shen, C.T. Lim, G.V. Subba Rao, B.V.R. Chowdari, Adv. Funct. Mater. 17 (15) (2007) 2792.
[87] M.D. Levi, G. Salitra, B. Markovsky, H. Teller, D. Aurbach, U. Heider, L. Heider, J. Electrochem. Soc. 146 (4) (1999) 1279.
[88] H. Li, H. Zhou, Chem. Commun. 48 (9) (2012) 1201.
[89] Y.J. Lee, H. Yi, W.-J. Kim, K. Kang, D.S. Yun, M.S. Strano, G. Ceder, A.M. Belcher, Science 324 (5930) (2009) 1051.
[90] H. Göktepe, Res. Chem. Intermed. 39 (7) (2013) 2979.
[91] H. Tukamoto, A.R. West, J. Electrochem. Soc. 144 (9) (1997) 3164.
[92] Z. Wang, D. Luan, S. Madhavi, Y. Hu, X.W. Lou, Energy Environ. Sci. 5 (2012) 5252.
[93] W. Zhou, J. Zhu, C. Cheng, J. Liu, H. Yang, C. Cong, C. Guan, X. Jia, H.J. Fan, Q. Yan, C.M. Li, T. Yu, Energy Environ. Sci. 4 (12) (2011) 4954.
[94] Y. Ma, G. Ji, J.Y. Lee, J. Mater. Chem. 21 (34) (2011) 13009.
[95] J. Jaidev, R.I. Jafri, A.K. Mishra, S. Ramaprabhu, J. Mater. Chem. 21 (44) (2011) 17601.
[96] Y. Hou, Y. Cheng, T. Hobson, J. Liu, Nano Lett. 10 (7) (2010) 2727.
[97] R.K. Sharma, A. Karakoti, S. Seal, L. Zhai, J. Power Sources 195 (4) (2010) 1256.
[98] D. Ahn, Y.-M. Koo, M.G. Kim, N. Shin, J. Park, J. Eom, J. Cho, T.J. Shin, J. Phys. Chem. C 114 (8) (2010) 3675.
[99] H. Cheng, Z. Lu, J. Deng, C. Chung, K. Zhang, Y. Li, Nano Res. 3 (12) (2010) 895.
[100] J. Zhu, Z. Yin, D. Yang, T. Sun, H. Yu, H.E. Hoster, H.H. Hng, H. Zhang, Q. Yan, Energy Environ. Sci. 6 (3) (2013) 987.
[101] J. Yang, J. Wang, X. Li, D. Wang, J. Liu, G. Liang, M. Gauthier, Y. Li, D. Geng, R. Li, X. Sun, J. Mater. Chem. 22 (15) (2012) 7537.
[102] X. Zhu, Y. Zhu, S. Murali, M.D. Stoller, R.S. Ruoff, ACS Nano 5 (4) (2011) 3333.
[103] X. Zhao, C.M. Hayner, H.H. Kung, J. Mater. Chem. 21 (43) (2011) 17297.
[104] Z.-S. Wu, W. Ren, D.-W. Wang, F. Li, B. Liu, H.-M. Cheng, ACS Nano 4 (10) (2010) 5835.
[105] A. Lewandowski, A. Świderska-Mocek, J. Power Sources 194 (2) (2009) 601.
[106] M. Afzal, M. Saleem, M.T. Mahmood, J. Chem. Eng. Data 34 (3) (1989) 339.
[107] W.J. Dunning, W.J. Shutt, Trans. Faraday Soc. 34 (0) (1938) 467.
[108] J.T. Dudley, D.P. Wilkinson, G. Thomas, R. LeVae, S. Woo, H. Blom, C. Horvath, M.W. Juzkow, B. Denis, P. Juric, P. Aghakian, J.R. Dahn, J. Power Sources 35 (1) (1991) 59.
[109] K. Xu, Chem. Rev. 104 (10) (2004) 4303.
[110] A.B. McEwen, S.F. McDevitt, V.R. Koch, J. Electrochem. Soc. 144 (4) (1997) L84.
[111] J. Read, J. Electrochem. Soc. 153 (1) (2006) A96.
[112] M. Galiński, A. Lewandowski, I. Stępniak, Electrochim. Acta 51 (26) (2006) 5567.
[113] T. Singh, A. Kumar, J. Phys. Chem. B 112 (41) (2008) 12968.
[114] T. Eriksson, A.M. Andersson, A.G. Bishop, C. Gejke, T. Gustafsson, J.O. Thomas, J. Electrochem. Soc. 149 (1) (2002) A69.
[115] X.L. Li, Y.L. Zhang, H.F. Song, K. Du, H. Wang, H.Y. Li, J.M. Huang, Int. J. Electrochem. Sci. 7 (2012) 7111.
[116] G. Du, J. Wang, Z. Guo, Z. Chen, H. Liu, Mater. Lett. 65 (9) (2011) 1319.
[117] L. Wei, M. Sevilla, A.B. Fuertes, R. Mokaya, G. Yushin, Adv. Funct. Mater. 22 (4) (2012) 827.
[118] T. Bordjiba, D. Belanger, J. Electrochem. Soc. 156 (5) (2009) A378.
[119] T.R. Jow, M.B. Marx, J.L. Allen, J. Electrochem. Soc. 159 (5) (2012) A604.
[120] M. Kaneko, M. Nakayama, Y. Wakizaka, K. Kanamura, M. Wakihara, Electrochim. Acta 53 (28) (2008) 8196.
[121] A. Nyman, M. Behm, G. Lindbergh, Electrochim. Acta 53 (22) (2008) 6356.
[122] J. Newman, K.E. Thomas, H. Hafezi, D.R. Wheeler, J. Power Sources 119–121 (0) (2003) 838.
[123] C. Hellwig, S. Sörgel, W.G. Bessler, ECS Trans. 35 (32) (2011) 215.
[124] P.B. Balbuena, Y. Wang (Eds.), Lithium-Ion Batteries: Solid-Electrolyte Interphase, Imperial College Press, London, 2004.
[125] A.M. Andersson. Doctor of Philosophy, Uppsala University, 2001.
[126] K. Edström, T. Gustafsson, J.O. Thomas, Electrochim. Acta 50 (2–3) (2004) 397.
[127] J.S. Gnanaraj, R.W. Thompson, S.N. Iaconatti, J.F. DiCarlo, K.M. Abraham, Electrochem. Solid-State Lett. 8 (2) (2005) A128.
[128] H. Zhang, J. Wang, Y. Chen, Z. Wang, S. Wang, Electrochim. Acta 105 (0) (2013) 69.
[129] F. Ataherian, N.-L. Wu, J. Electrochem. Soc. 158 (4) (2011) A422.
[130] B. Ravdel, K.M. Abraham, R. Gitzendanner, J. DiCarlo, B. Lucht, C. Campion, J. Power Sources 119–121 (0) (2003) 805.
[131] C. Wang, A.J. Appleby, F.E. Little, J. Electroanal. Chem. 497 (1–2) (2001) 33.
[132] W.Av. Schalkwijk, B. Scrosati (Eds.), Advances in Lithium-Ion Batteries, Kluwer Academic Publishers, New York, 2002.
[133] A. Izadi-Najafabadi, D.N. Futaba, S. Iijima, K. Hata, J. Am. Chem. Soc. 132 (51) (2010) 18017.
[134] A. Celzard, F. Collas, J.F. Marêché, G. Furdin, I. Rey, J. Power Sources 108 (1–2) (2002) 153.
[135] B. Kang, G. Ceder, Nature 458 (7235) (2009) 190.
[136] W. Lu, A. Goering, L. Qu, L. Dai, PCCP 14 (35) (2012) 12099.
[137] C.K. Chan, H. Peng, G. Liu, K. McIlwrath, X.F. Zhang, R.A. Huggins, Y. Cui, Nat. Nano 3 (1) (2008) 31.
[138] P.L. Taberna, S. Mitra, P. Poizot, P. Simon, J.M. Tarascon, Nat. Mater. 5 (7) (2006) 567.
[139] J.-H. Kim, K.H. Lee, L.J. Overzet, G.S. Lee, Nano Lett. 11 (7) (2011) 2611.
[140] X. Jia, C. Yan, Z. Chen, R. Wang, Q. Zhang, L. Guo, F. Wei, Y. Lu, Chem. Commun. 47 (34) (2011) 9669.
[141] H. Gullapalli, A.L. Mohana Reddy, S. Kilpatrick, M. Dubey, P.M. Ajayan, Small 7 (12) (2011) 1697.
[142] J.J. Yoo, K. Balakrishnan, J. Huang, V. Meunier, B.G. Sumpter, A. Srivastava, M. Conway, A.L. Mohana Reddy, J. Yu, R. Vajtai, P.M. Ajayan, Nano Lett 11 (4) (2011) 1423.
[143] M.F. El-Kady, V. Strong, S. Dubin, R.B. Kaner, Science 335 (6074) (2012) 1326.
[144] X. Yang, J. Zhu, L. Qiu, D. Li, Adv. Mater. 23 (25) (2011) 2833.
[145] D.-W. Wang, F. Li, M. Liu, G.Q. Lu, H.-M. Cheng, Angew. Chem. Int. Ed. 47 (2) (2008) 373.
[146] H. Zhang, G. Cao, Y. Yang, Energy Environ. Sci. 2 (9) (2009) 932.
[147] H. Zhang, G. Cao, Z. Wang, Y. Yang, Z. Shi, Z. Gu, Nano Lett 8 (9) (2008) 2664.
[148] Q. Li, Z.-L. Wang, G.-R. Li, R. Guo, L.-X. Ding, Y.-X. Tong, Nano Lett 12 (7) (2012) 3803.
[149] J. Liu, J. Jiang, M. Bosman, H.J. Fan, J. Mater. Chem. 22 (6) (2012) 2419.
[150] S. Dong, X. Chen, L. Gu, X. Zhou, L. Li, Z. Liu, P. Han, H. Xu, J. Yao, H. Wang, X. Zhang, C. Shang, G. Cui, L. Chen, Energy Environ. Sci. 4 (9) (2011) 3502.
[151] K. Evanoff, J. Khan, A.A. Balandin, A. Magasinski, W.J. Ready, T.F. Fuller, G. Yushin, Adv. Mater. 24 (4) (2012) 533.
[152] A. Gohier, B. Laïk, K.-H. Kim, J.-L. Maurice, J.-P. Pereira-Ramos, C.S. Cojocaru, P.T. Van, Adv. Mater. 24 (19) (2012) 2592.
[153] P.M. Ajayan, O. Stephan, C. Colliex, D. Trauth, Science 265 (5176) (1994) 1212.
[154] W.Z. Li, S.S. Xie, L.X. Qian, B.H. Chang, B.S. Zou, W.Y. Zhou, R.A. Zhao, G. Wang, Science 274 (5293) (1996) 1701.
[155] W. Li, H. Zhang, C. Wang, Y. Zhang, L. Xu, K. Zhu, S. Xie, Appl. Phys. Lett. 70 (20) (1997) 2684.
[156] G. Che, B.B. Lakshmi, C.R. Martin, E.R. Fisher, R.S. Ruoff, Chem. Mater. 10 (1) (1998) 260.
[157] B.D. Yao, N. Wang, J. Phys. Chem. B 105 (46) (2001) 11395.
[158] S. Talapatra, S. Kar, S.K. Pal, R. Vajtai, L. Ci, P. Victor, M.M. Shaijumon, S. Kaur, O. Nalamasu, P.M. Ajayan, Nat. Nano 1 (2) (2006) 112.
[159] G. Che, B.B. Lakshmi, E.R. Fisher, C.R. Martin, Nature 393 (6683) (1998) 346.
[160] H.-J. Ahn, J.I. Sohn, Y.-S. Kim, H.-S. Shim, W.B. Kim, T.-Y. Seong, Electrochem. Commun. 8 (4) (2006) 513.
[161] W.-J. Yu, P.-X. Hou, L.-L. Zhang, F. Li, C. Liu, H.-M. Cheng, Chem. Commun. 46 (45) (2010) 8576.
[162] G. Zheng, Y. Yang, J.J. Cha, S.S. Hong, Y. Cui, Nano Lett. 11 (10) (2011) 4462.
[163] W.-J. Yu, P.-X. Hou, F. Li, C. Liu, J. Mater. Chem. 22 (27) (2012) 13756.
[164] M.M. Shaijumon, F.S. Ou, L. Ci, P.M. Ajayan, Chem. Commun. 0 (20) (2008) 2373.
[165] A.L.M. Reddy, S.R. Gowda, M.M. Shaijumon, P.M. Ajayan, Adv. Mater. 24 (37) (2012) 5045.
[166] M.G. Hahm, A. Leela Mohana Reddy, D.P. Cole, M. Rivera, J.A. Vento, J. Nam, H.Y. Jung, Y.L. Kim, N.T. Narayanan, D.P. Hashim, C. Galande, Y.J. Jung, M. Bundy, S. Karna, P.M. Ajayan, R. Vajtai, Nano Lett. 12 (11) (2012) 5616.
[167] A.L.M. Reddy, M.M. Shaijumon, S.R. Gowda, P.M. Ajayan, Nano Lett. 9 (3) (2009) 1002.
[168] A. Okamoto, I. Gunjishima, T. Inoue, M. Akoshima, H. Miyagawa, T. Nakano, T. Baba, M. Tanemura, G. Oomi, Carbon 49 (1) (2011) 294.
[169] H. Zhang, G.P. Cao, Y.S. Yang, Nanotechnology 18 (19) (2007) 195607.
[170] Y. Honda, T. Haramoto, M. Takeshige, H. Shiozaki, T. Kitamura, M. Ishikawa, Electrochem. Solid-State Lett. 10 (4) (2007) A106.
[171] X. Cui, F. Hu, W. Wei, W. Chen, Carbon 49 (4) (2011) 1225.
[172] Y. Naoki, et al., Nanotechnology 19 (24) (2008) 245607.
[173] B. Kim, H. Chung, K.S. Chu, H.G. Yoon, C.J. Lee, W. Kim, Synth. Met. 160 (7-8) (2010) 584.
[174] G. Atthipalli, Y. Tang, A. Star, J.L. Gray, Thin Solid Films 520 (5) (2011) 1651.
[175] S.P. Patole, H.-I. Kim, J.-H. Jung, A.S. Patole, H.-J. Kim, I.-T. Han, V.N. Bhoraskar, J.-B. Yoo. Carbon, 49(11): 3522.
[176] S. Li, Y. Luo, W. Lv, W. Yu, S. Wu, P. Hou, Q. Yang, Q. Meng, C. Liu, H.-M. Cheng, Adv. Energy Mater. 1 (4) (2011) 486.
[177] H. Zhang, G. Cao, Z. Wang, Y. Yang, Z. Gu, Carbon 46 (5) (2008) 822.
[178] E. Krämer, S. Passerini, M. Winter, ECS Electrochem. Lett. 1 (5) (2012) C9.
[179] L. Wei, W. Jiang, Y. Yuan, K. Goh, D. Yu, L. Wang, Y. Chen, J. Solid State Chem. 224 (2015) 45.
[180] Y. Zhu, L. Li, C. Zhang, G. Casillas, Z. Sun, Z. Yan, G. Ruan, Z. Peng, A.-R.O. Raji, C. Kittrell, R.H. Hauge, J.M. Tour, Nat. Commun. 3 (2012) 1225.
[181] C.-C. Su, S.-H. Chang, Mater. Lett. 65 (17-18) (2011) 2700.
[182] F. Lou, H. Zhou, F. Vullum-Bruer, T.D. Tran, D. Chen, J. Mater. Chem. A 1 (11) (2013) 3757.
[183] F. Huang, E. Vanhaecke, D. Chen, Catal. Today 150 (1-2) (2010) 71.
[184] F. Lou, H. Zhou, T.D. Tran, M.E. Melandsø Buan, F. Vullum-Bruer, M. Rønning, J.C. Walmsley, D. Chen, ChemSusChem 7 (5) (2014) 1335.
[185] E. Vanhaecke, F. Huang, Y. Yu, M. Rønning, A. Holmen, D. Chen, Top. Catal. 54 (13) (2011) 986.
[186] F. Lou, H. Zhou, F. Vullum-Bruer, T.D. Tran, D. Chen, J. Energy Chem. 22 (1) (2013) 78.
[187] Y. Fovet, J.-Y. Gal, F. Toumelin-Chemla, Talanta 53 (5) (2001) 1053.
[188] S.-T. Myung, Y. Sasaki, S. Sakurada, Y.-K. Sun, H. Yashiro, Electrochim. Acta 55 (1) (2009) 288.
[189] K. Jurewicz, S. Delpeux, V. Bertagna, F. Béguin, E. Frackowiak, Chem. Phys. Lett. 347 (1-3) (2001) 36.
[190] E. Frackowiak, V. Khomenko, K. Jurewicz, K. Lota, F. Béguin, J. Power Sources 153 (2) (2006) 413.
[191] G.A. Snook, P. Kao, A.S. Best, J. Power Sources 196 (1) (2011) 1.

[192] Y. Zhou, Z.-Y. Qin, L. Li, Y. Zhang, Y.-L. Wei, L.-F. Wang, M.-F. Zhu, Electrochim. Acta 55 (12) (2010) 3904.
[193] L. Li, Z.-Y. Qin, X. Liang, Q.-Q. Fan, Y.-Q. Lu, W.-H. Wu, M.-F. Zhu, J. Phys. Chem. C 113 (14) (2009) 5502.
[194] H. Zhang, G. Cao, W. Wang, K. Yuan, B. Xu, W. Zhang, J. Cheng, Y. Yang, Electrochim. Acta 54 (4) (2009) 1153.
[195] H. Zhang, G. Cao, Z. Wang, Y. Yang, Z. Shi, Z. Gu, Electrochem. Commun. 10 (7) (2008) 1056.
[196] V.V. Tat'yana, N.E. Oleg, Russian Chem. Rev. 66 (5) (1997) 443.
[197] M. Hughes, M.S.P. Shaffer, A.C. Renouf, C. Singh, G.Z. Chen, D.J. Fray, A.H. Windle, Adv. Mater. 14 (5) (2002) 382.
[198] J.H. Chen, Z.P. Huang, D.Z. Wang, S.X. Yang, W.Z. Li, J.G. Wen, Z.F. Ren, Synth. Met. 125 (3) (2001) 289.
[199] Y. Xu, S. Zhuang, X. Zhang, P. He, Y. Fang, Chin. Sci. Bull. 56 (35) (2011) 3823.
[200] K. Lota, V. Khomenko, E. Frackowiak, J. Phys. Chem. Solids 65 (2–3) (2004) 295.
[201] J. Chen, Y. Liu, A.I. Minett, C. Lynam, J. Wang, G.G. Wallace, Chem. Mater. 19 (15) (2007) 3595.
[202] P. Poizot, S. Laruelle, S. Grugeon, L. Dupont, J.M. Tarascon, Nature 407 (6803) (2000) 496.
[203] Y.-S. Li, I.W. Sun, J.-K. Chang, C.-J. Su, M.-T. Lee, J. Mater. Chem. 22 (13) (2012) 6274.
[204] H. Jiang, L. Yang, C. Li, C. Yan, P.S. Lee, J. Ma, Energy Environ. Sci. 4 (5) (2011) 1813.
[205] X. Du, C. Wang, M. Chen, Y. Jiao, J. Wang, J. Phys. Chem. C 113 (6) (2009) 2643.
[206] M.B. Sassin, A.N. Mansour, K.A. Pettigrew, D.R. Rolison, J.W. Long, ACS Nano 4 (8) (2010) 4505.
[207] H. Xia, M. Lai, L. Lu, J. Mater. Chem. 20 (33) (2010) 6896.
[208] W. Tang, X. Yang, Z. Liu, K. Ooi, J. Mater. Chem. 13 (12) (2003) 2989.
[209] J. Li, Y. Zhao, N. Wang, Y. Ding, L. Guan, J. Mater. Chem. 22 (26) (2012) 13002.
[210] F. Jiao, P.G. Bruce, Adv. Mater. 19 (5) (2007) 657.
[211] B. Ammundsen, J. Paulsen, Adv. Mater. 13 (12-13) (2001) 943.
[212] Z. Fan, J. Chen, B. Zhang, B. Liu, X. Zhong, Y. Kuang, Diamond Relat. Mater. 17 (11) (2008) 1943.
[213] V.K. Sharma, Adv. Environ. Res. 6 (2) (2002) 143.
[214] M.B. Sassin, C.N. Chervin, D.R. Rolison, J.W. Long, Acc. Chem. Res. 46 (5) (2013) 1062.
[215] C.H. Jiang, S.X. Dou, H.K. Liu, M. Ichihara, H.S. Zhou, J. Power Sources 172 (1) (2007) 410.
[216] M.S. Islam, R. Dominko, C. Masquelier, C. Sirisopanaporn, A.R. Armstrong, P.G. Bruce, J. Mater. Chem. 21 (27) (2011) 9811.
[217] D. Lv, W. Wen, X. Huang, J. Bai, J. Mi, S. Wu, Y. Yang, J. Mater. Chem. 21 (26) (2011) 9506.
[218] H. Zhou, F. Lou, P.E. Vullum, M.-A. Einarsrud, D. Chen, F. Vullum-Bruer, Nanotechnology 24 (43) (2013) 435703.
[219] Y. Yang, M.T. McDowell, A. Jackson, J.J. Cha, S.S. Hong, Y. Cui, Nano Lett 10 (4) (2010) 1486.
[220] A. Magasinski, P. Dixon, B. Hertzberg, A. Kvit, J. Ayala, G. Yushin, Nat. Mater. 9 (4) (2010) 353.
[221] W. Wang, R. Epur, P.N. Kumta, Electrochem. Commun. 13 (5) (2011) 429.
[222] W. Lu, L. Qu, K. Henry, L. Dai, J. Power Sources 189 (2) (2009) 1270.
[223] S. Rakesh, et al., Nanotechnology 20 (39) (2009) 395202.
[224] V.L. Pushparaj, M.M. Shaijumon, A. Kumar, S. Murugesan, L. Ci, R. Vajtai, R.J. Linhardt, O. Nalamasu, P.M. Ajayan, Proc. Natl. Acad. Sci. 104 (34) (2007) 13574.
[225] H. Zhang, G. Cao, Y. Yang, J. Power Sources 172 (1) (2007) 476.
[226] H. Zhang, G. Cao, Y. Yang, Z. Gu, Carbon 46 (1) (2008) 30.
[227] J. Kim, A. Manthiram, Nature 390 (6657) (1997) 265.
[228] D. Aurbach, B. Markovsky, A. Rodkin, M. Cojocaru, E. Levi, H.-J. Kim, Electrochim. Acta 47 (12) (2002) 1899.
[229] K.M. Shaju, P.G. Bruce, Chem. Mater. 20 (17) (2008) 5557.
[230] Y.-L. Ding, J. Xie, G.-S. Cao, T.-J. Zhu, H.-M. Yu, X.-B. Zhao, Adv. Funct. Mater. 21 (2) (2011) 348.
[231] D.T. Welna, L. Qu, B.E. Taylor, L. Dai, M.F. Durstock, J. Power Sources 196 (3) (2011) 1455.
[232] G.X. Wang, J. Yao, H.K. Liu, S.X. Dou, J.H. Ahn, Met. Mater. Int. 12 (5) (2006) 413.
[233] J. Guo, Q. Liu, C. Wang, M.R. Zachariah, Adv. Funct. Mater. 22 (4) (2011) 803.
[234] Y. Zhu, S. Murali, W. Cai, X. Li, J.W. Suk, J.R. Potts, R.S. Ruoff, Adv. Mater. 22 (35) (2010) 3906.
[235] Y. Wu, P. Qiao, T. Chong, Z. Shen, Adv. Mater. 14 (1) (2002) 64.
[236] Z. Bo, S. Mao, Z. Jun Han, K. Cen, J. Chen, K. Ostrikov, Chem. Soc. Rev. 44 (8) (2015) 2108.
[237] S. Jin, N. Li, H. Cui, C. Wang, Nano Energy 2 (6) (2013) 1128.
[238] J.R. Miller, R.A. Outlaw, B.C. Holloway, Science 329 (5999) (2010) 1637.
[239] X. Xiao, P. Liu, J.S. Wang, M.W. Verbrugge, M.P. Balogh, Electrochem. Commun. 13 (2) (2011) 209.
[240] H. Kim, Z. Wen, K. Yu, O. Mao, J. Chen, J. Mater. Chem. 22 (31) (2012) 15514.
[241] R. Thomas, K. Yellareswar Rao, G. Mohan Rao, Electrochim. Acta 108 (0) (2013) 458.
[242] C. Zhang, Z. Peng, J. Lin, Y. Zhu, G. Ruan, C.-C. Hwang, W. Lu, R.H. Hauge, J.M. Tour, ACS Nano 7 (6) (2013) 5151.
[243] B. Li, S. Li, J. Liu, B. Wang, S. Yang, Nano Lett 15 (5) (2015) 3073.